Investigation of Sub-Pitch Spatial Resolution for Pixelated CZT X-Ray Detector

INVESTIGATION OF SUB-PITCH SPATIAL RESOLUTION FOR PIXELATED CZT X-RAY DETECTOR

BY

YIKE LI, B.Sc., (Electronic Science and Technology)

Tianjin University, Tianjin, China

A THESIS

SUBMITTED TO THE DEPARTMENT OF ELECTRICAL & COMPUTER ENGINEERING

AND THE SCHOOL OF GRADUATE STUDIES

OF MCMASTER UNIVERSITY

IN PARTIAL FULFILMENT OF THE REQUIREMENTS

FOR THE DEGREE OF

MASTER OF APPLIED SCIENCE

Master of Applied Science (2016)   McMaster University

(Electrical & Computer Engineering)   Hamilton, Ontario, Canada

TITLE: Investigation of Sub-Pitch Spatial Resolution for Pixe-
                    lated CZT X-Ray Detector

AUTHOR: Yike Li

                    M.A.Sc., (Precision Instrument and Machinery)

                    Shanghai Jiao Tong University, Shanghai, China

SUPERVISOR: Dr. Xiaolin Wu

NUMBER OF PAGES: xii, 90

DEDICATED

WITH LOVE AND AFFECTION

TO MY FATHER

AND

TO ALL THOSE HONOURABLE FIGHTERS

WHO

THROUGHOUT THE LONG PAST DAYS

COMBATED OR ARE COMBATING AGAINST CANCER

WITH

THEIR ADMIRABLE COURAGE AND CONVICTION

AS WELL AS

ENDLESS LOVE OF LIFE

Abstract

As everyone knows, cancer is one of the greatest health enemies of mankind and became a major public health problem all over the world. Moreover, lung cancer is the most common global cancer leading to more than 1.3 million estimated deaths annually worldwide. Breast cancer is the most common cancer and the 2nd leading cause of death from in women in the US, Canada, and China. Therefore an instrument for the early diagnosis and monitoring of cancers in areas such as lung and breast is immensely important and necessary.

The cadmium zinc telluride (CZT) semiconductor is a kind of novel radiation detector that can provide detailed information about spatial position. Also, the energy resulting from interactions between the radiation and the CZT material can also be assessed giving this type of detector added value in disease evaluation. A great deal of work on CZT detectors has been done for breast CT scanning. Furthermore, the CZT detector is also a potential solution for problems in lung cancer CT evaluation where the lack of energy information and high radiation exposure are less than ideal. Since sub-millimetre spatial resolution is required for post-contrast thoracic CT assessment, and 100 μm or better is critical for breast CT, the investigation of spatial resolution for CZT detectors is essential.

In this thesis, the interactions within CZT detectors were analyzed. The influence

of different configurations, including adjustment of anode size, gap size, detector thickness and bias voltage, were discussed. Next the methods to evaluate two kinds of signals (collected and transit signals), are provided in Chapter 2. In Chapter 3, an intensity difference method and an intensity ratio method for estimating the sub-pitch spatial resolution were described in detail. Finally, a detector spatial resolution between 10 μm and 20 μm was achieved using the collecting signal intensities ratio method and a 4 mm thick CZT detector with gap size of $g = 50$ μm and bias voltage of $V = 300V$.

Future work should focus on the contributions from characteristic X-rays emitted from cadmium and tellurium atoms. Also, the work presented was only on pixelated arrays and further assessment of cross-strip electrode detectors could also be of bene-fit. Lastly based on simulations done in this thesis all photons were assumed to strike the cathode at 90 degrees. Future work should also include non-orthogonal directions for photons.

Acknowledgements

Well over the past two years, many wonderful people have lent me a helping hand. Without you, I would not be able to be here right now.

I would like to thank my supervisor, Dr. Hao Peng, and my co-supervisor, Dr. Xiaolin Wu. They have supported me from funding to lab equipment to sharing some useful books with me, while also giving me the chance to work hard for my dream.

My sincerest appreciation also goes out to my colleagues and friends for the invaluable supports. Thank you, Mr. Ruibin Dai and Mrs. Xiaoqing Zheng for taking the time to have discussions with me about my projects; Mr. Yicheng Liang for installing software in Ubuntu for me time after time again; and Mr. Irfan Khan for helping me a lot with my English skills and thesis review.

To Mrs. Cheryl Gies, our obliging Graduate Administrative Assistant, and Dr. Michael Noseworthy, a respectable professor and mentor to me, I owe my deepest respect and gratitude. Without your selfless and devoted help, I could not imagine how I would be feeling in my last few days at McMaster University.

Most importantly, I feel very much blessed and thankful for my parents. To my affectionate mother, a brave and strong woman, who loves me, understands me and supports me; and to my memorable father, a great and honourable man, who loved me, inspired me and led me into this domain of medical imaging instrument.

I am proud I did not let you down.

Notation and abbreviations

ARSR   Age-Standardized Relative Survival Ratio

CdTe   Cadmium Telluride

CS   Compton Scattering

CT   Computed Tomography

CZT   Cadmium Zinc Telluride

DOI   Depth of Interaction

FOV   Field of View

FWHM   Full Width at Half Maximum

GATE   Geant4 Application to Tomographic Emission

Geant4   GEometry ANd Tracking

HU   Hounsfield Units

LSF   Line Spread Function

NLST   National Lung Screening Trial

PE   Photoelectric Effect

PMT   Photomultiplier Tube

PSF   Point Spread Function

RMS   Root Mean Square

RS   Rayleigh Scattering

Contents

List of Figures

List of Tables

Chapter 1

Introduction

As people are paying increased attention to their own health in this era of science and technology explosion, the demand for techniques that offer precise and prompt diagnosis has become increasingly more important. Since the first head computed axial tomography (CAT) scanner introduced in 1972, the CAT scan (now called CT) has matured greatly and become more and more technically sophisticated. Furthermore, CT has proven itself as an invaluable tool helping us meet many clinical applications, such as cancer diagnosis, trauma assessment, osteoporosis screening, and real-time cardiac tomography, to name a few. The CT scanner is used not only in medicine but also in many other industrial applications, such as soil core analysis and nondestructive testing (Bushberg *et al.*, 2003). It is not hard to see that research and development to improve CT technology has and likely will be a 'hot research area' likely for decades to come.

1.1 CT Principle

A CT scan makes use of computer-processed data from many X-ray images taken at multiple incremental angles around the object to produce cross-sectional (tomographic) images,

allowing a user to see the inside without cutting. This is classified as a minimally invasive technology because although there is no cutting there is still a dose of ionizing radiation. To acquire tomographic images of an object, a CT scanner contains an X-ray generator (x-ray tube), which yields X-rays of a certain energy, and a series of detectors, which collect X-rays following penetration and passage through the object. To take images from different angles, a CT scanner uses a 'slip ring style' gantry to allow the X-ray source and detectors to rotate around the object.

In this process, a line penetrating the object, connecting between the focal point in the X-ray source and a point on the detector is called a *ray*, and a series of rays that run through the object is called a *projection* or a *view*, Figure 1.1. According to Radon's treatise, published in 1917 (Radon, 2005), if there are enough rays, coronal anatomical images of the object could be obtained with a series of side projections around it (Bushberg *et al.*, 2003). This is based on several laws and assumptions.
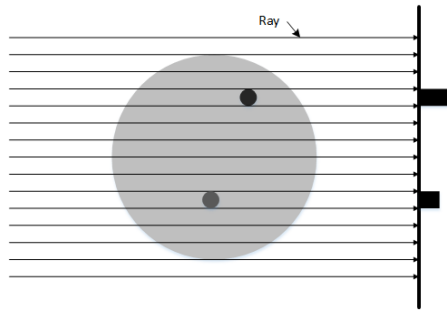
Figure 1.1: Schematic representation of one projection in CT scanning. A ray is a line penetrating the object and a series of rays that run through the object from one angle is called a projection.

1.1.1 Lambert-Beer's Law

Radiation, of a particular energy, captured by a detector following a passage through a homogeneous object, becomes attenuated during the passage. This attenuation is always in

the form of reducing the number of photons and usually is classified by a single coefficient,

μ in the top of Figure 1.2.
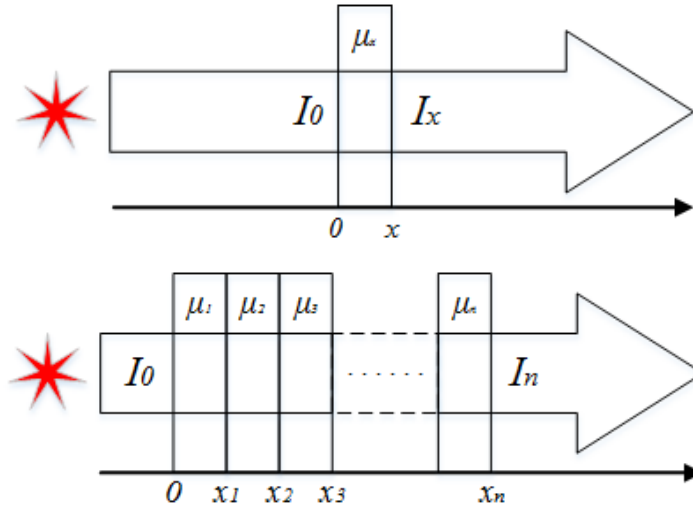
Figure 1.2: Mathematical model of monochromatic X-ray attenuation. According to the *Lambert-Beer Law*, x-rays are attenuated in an exponential fashion according to the material properties and distance through which the photons pass. In the top figure, attenuation is represented by one decay coefficient while attenuation through a series of blocks (bottom) would be related to each block's properties.

The total attenuation of a monochromatic X-ray beam can be calculated by the *Lambert-Beer* Law of attenuation (Buzug, 2008):

$$I_x = I_0 e^{-\mu_x} \tag{1.1}$$

where I is the radiation intensity and x is the position along the radiation projection. High-density materials block more radiation, resulting in fewer photons (i.e. more attenuation) at the detector, Figure 1.1.

1.1.2 CT Values

In CT, axially acquired images are represented by different grey scale values indicating different tissue types inside the body, each with differing attenuation values, μ. Attenuation values are converted into CT values with its definition as:

$$Value_{CT} = 1000 \cdot \frac{\mu - \mu_{water}}{\mu_{water}} \qquad (1.2)$$

In honour of *Sir* Godfrey Newbold Hounsfield, the inventor of the CT scanner and Laureate of the Nobel Prize in Medicine in 1979, CT values are described as Hounsfield units (HU). Tab. 1.1 shows the CT values of common bodily tissues, in which one HU change means a 0.1% attenuation coefficient change of the different attenuation coefficients between air and water.

Table 1.1: The CT values of common substances. The CT value of water is set to be 0. The data was extracted from (Bushberg and Boone, 2011).

Substance	Air	Lung	Fat	Water	Soft Tissue	Bone
CT value (HU)	-1000	-500	-100 to -50	0	100 to 300	700 to 3000

1.1.3 Voxel

There are two restricted conditions in *Lambert-Beer's* Law, which summarized state that the X-ray is monochromatic passing through an object that is homogeneous. Thus, in order to apply *Lambert-Beer's* Law, an object is cut into thin axially acquired slices, and then a slice is divided into tiny volume elements, called voxels, shown in Figure 1.3.

Each voxel is assumed uniform since it is [typically] small enough, meaning it has a single CT Value. Considering a ray passing through the object within the slice, it would penetrate every voxel along its trajectory and the radiation density would be attenuated 'bit-by-bit'
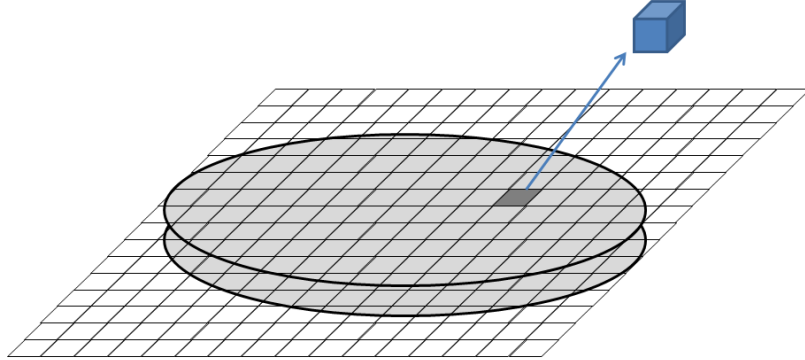
Figure 1.3: Schematic representation of the definition of a voxel. A voxel is a volume element that constitutes a notional three-dimensional space.

as it passes through each voxel. In other words, *Lambert-Beer's* Law (Equation 1.1) would be applied several times as:

$$I_n = I_{n-1}e^{-\mu_n} \tag{1.3}$$

$$\mu_n = \ln(\frac{I_{n-1}}{I_n}) \tag{1.4}$$

where I_{n-1} and I_n represent the intensities of the radiation after the *n-1*th and the *n*th voxel respectively, and μ_n is the attenuation coefficient of the *n*th voxel. Therefore, the final intensity of the radiation shown in the bottom of Figure 1.2 is given by:

$$I_n = I_0e^{-\mu} \tag{1.5}$$

$$\mu = \mu_1 + \mu_2 + \mu_3 + \cdots + \mu_n \tag{1.6}$$

Theoretically, all the voxel CT values would all be solved if the projections for the slice were sufficient. Then the tomogram could be obtained, shown in Figure 1.4.
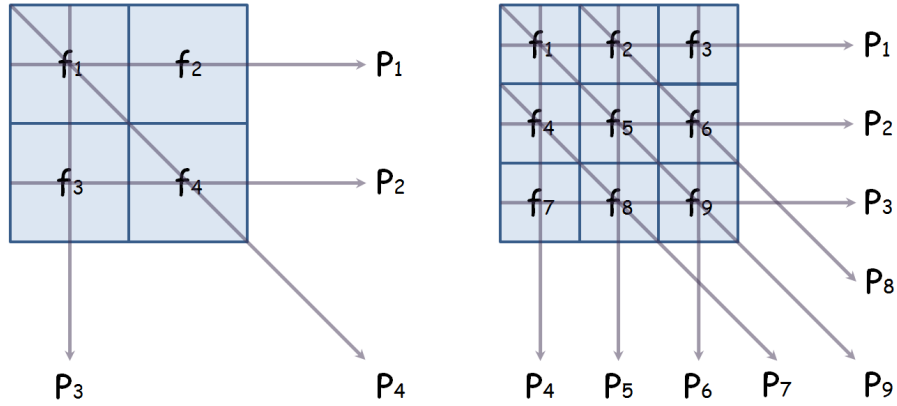
Figure 1.4: Schematic representation showing how we obtain CT values of each voxel by solving a linear system of equations of a set of projections. All four unknown CT values could be calculated exactly using four projections from three projection angles in the left figure. With a finer grid more CT values correspondingly will need more projections, as shown in the right figure.

1.2   Interaction of Radiation and Charged Particle

In medical imaging applications, the X-ray is a type of high-energy photon, which has energy ranging from 10 keV to 140 keV, subsequently losing energy as it passes through a patient's body. Sometimes, secondary electrons or X-ray photons might be produced by different kinds of interactions between the original X-ray photons and the matter within the patient and also the matter within the detectors themselves. A series of interactions caused by an original photon is called an event, no matter what kinds of or how many secondary particles are generated by these interactions. Generally, interactions between X-ray photons or the secondary particles, and matter include *photoelectric effect* (PE), *Compton scattering* (CS), *Rayleigh scattering* (RS), *atomic emissions*, and *ionization*.

1.2.1   Photoelectric Effect

The *photoelectric effect* is an atomic absorption process in which an incident photon looses all of its energy and disappears. In the process, an electron, called a photoelectron, is

ejected with a certain amount of kinetic energy E_{pe}, which equals the difference between the incident photon energy E_0 and the binding energy of the electron shell E_b (Cherry *et al.*, 2012). It is understood that the incident photon has transferred as much as its energy to the photoelectron and disappears as shown in Figure 1.5.

$$E_{pe} = E_0 - E_b \qquad (1.7)$$
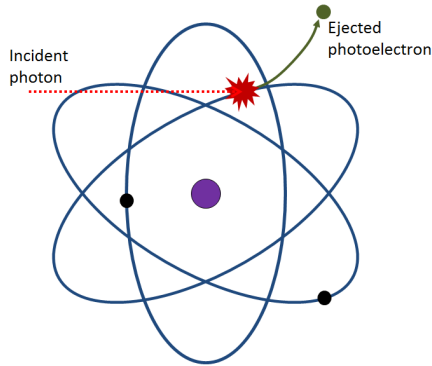
Figure 1.5: The *photoelectric effect* is an atomic absorption process in which an incident photon transfers all of its energy, disappears in the process, as a photoelectron gets ejected with a certain amount of kinetic energy. The Figure is reproduced based on (Cherry *et al.*, 2012)

At x-ray energies during running of the CT scanner, most interactions between X-ray photons detector materials are due to the *photoelectric effect* (Section 2.2.2). Thus, analysis of this behaviour is important in this thesis.

1.2.2 Compton Scattering

Unlike the *photoelectric effect*, *Compton scattering* does not result in elimination of the original incident photon but rather deflects it with a scattering angle θ thus generating a new electron called the *Compton recoil electron* (Figure 1.6). The energy of this scattered photon is related to the scattering angle θ between the scattered photon and the incident

photon.

The bigger the scattering angle θ, the less energy in the scattered photon, as described by Equation 1.8. For CT application, the highest intensity of Compton scattered photons would be toward the forward or backward direction, with a minimum at a $90°$ angle to the original direction of the incident photon (Cherry *et al.*, 2012) (Section 2.2.3). *Compton scattering* leads to a statistical error with radiation deflecting.

$$E_{sc} = E_0/[1 + (E_0/0.511)(1 - \cos\theta)] \tag{1.8}$$

$$E_{re} = E_0 - E_{sc} \tag{1.9}$$
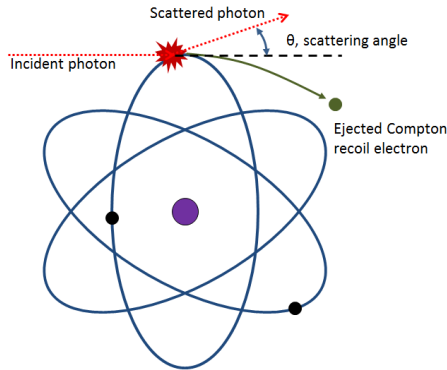
Figure 1.6: The *Compton scattering* is an energy transfer process in which an incident photon gives part of its energy and changes its direction of motion. Concurrently, a *Compton recoil electron* is ejected from the atom as well. The Figure is reproduced based on (Cherry *et al.*, 2012)

1.2.3   Rayleigh Scattering

Another interaction between matter and high energy photons is *Rayleigh scattering* or *coherent scattering*. *Rayleigh scattering* does not deposit any energy into matter, but rather only deflect the incident photon. Just like *Compton scattering*, *Rayleigh scattering* occupies

a certain proportion of the total number of radiation/matter interactions (Section 2.2.2), and it causes a statistical error after deflecting the trajectory of the radiation as well.

1.2.4 Atomic Emissions

When there is an empty position for an electron in one of the inner shells of atom due to some kind of interaction of radiation with the atom, such as *photoelectric effect*, *Compton scattering* or something else, an electron from an outer shell drops in to fill the position and releases a new photon or electron, which is called an *atomic emission*. Basically, there are two types of *atomic emissions*: *characteristic X-ray* and *Auger effect*.

1. *Characteristic X-Ray*

   A new photon, usually X-ray photon, emitted from the atom due to a vacancy on the inner shell was filled is called *characteristic radiation* or *characteristic X-ray* (Figure 1.7). The energy of this new photon equals the difference in energies between the binding energies of two shells exactly, which has an exact characteristic value for each element, and it might further cause another interaction within the matter.
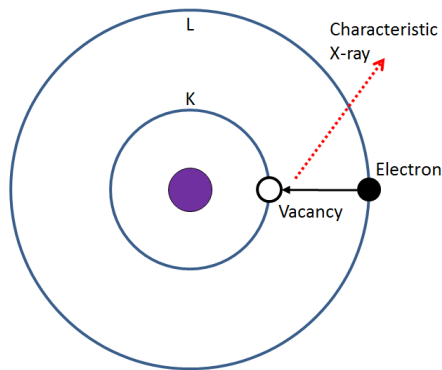
Figure 1.7: The *characteristic X-ray* is emitted when a vacancy on the inner shell is filled by an electron from an outer shell. The figure is reproduced based on (Cherry *et al.*, 2012)

2. *Auger Electron*

   Instead of a *characteristic X-ray*, an *Auger electron* is sometimes emitted out of the atom, through a processed called the *Auger effect*. Here an outer shell electron fills the vacancy of the inner shell, similarly to *characteristic radiation*, but the energy released during the effect is transferred to another electron and drives it out of the atom as an *Auger electron*, shown in Figure 1.8.
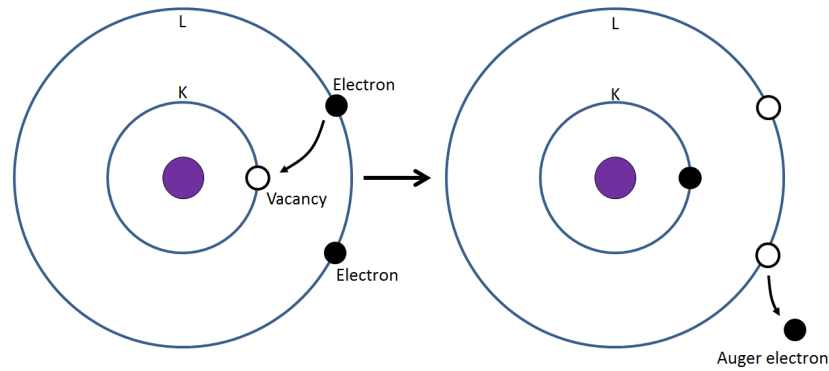
Figure 1.8: The *Auger electron* is emitted when a vacancy on the inner shell is filled by another electron from an outer shell. The figure is reproduced based on (Cherry *et al.*, 2012)

The vacancies left by *characteristic radiation* or an *Auger effect* could be filled by other electrons from outer shells and cause *atomic emissions* as well. The probability of an *atomic emission* between *characteristic radiation* and *Auger effect* depends on the atomic number, Z. Generally, for elements with higher atomic number (i.e. high Z nuclei), *characteristic radiation* is more likely to occur (Cherry *et al.*, 2012).

1.2.5   Ionization

Ionization is a kind of "collision" between a charged particle and atoms or molecules, in which the charged particle is attracted or repulsed by electrical forces, costing a part of

its energy to separate electrons from the atoms or molecules thus resulting in *ionization*, shown in Figure 1.9. As a charged particle travels through matter it leads to a continual stream of *ionization*. Thus an electron cloud is generated along its path within the matter. This is eventually collected by anodes and transferred into output signals of the detector (Cherry *et al.*, 2012).
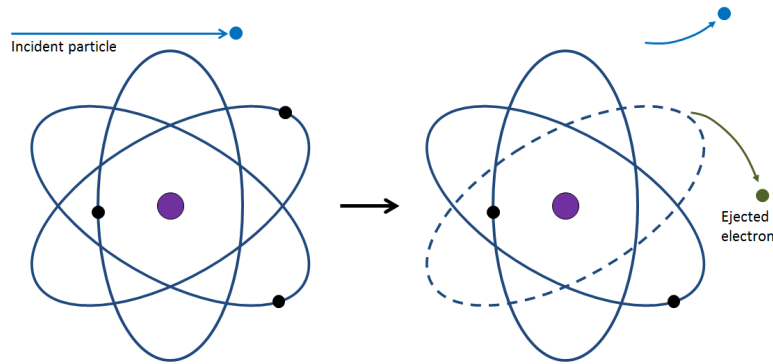
Figure 1.9: The *ionization* is a collision between a charged particle and atoms, in which the charged particle is attracted to or repulsed from the atom and transfers a part of its energy to an electron which then gets ejected from the atom. The figure is reproduced based on (Cherry *et al.*, 2012)

1.3   CT Development

CT has evolved for almost half a century with several generations being used for clinical applications. In addition to computational advancements, concomitant changes have occurred in acquisition geometry and detector technology.

1.3.1   Geometry Development

Through the evolution of CT history, according to the modes of detectors' movement and the kinds of X-ray emission, there have been eight generations of CT scanners marketed for clinical use (Bushberg and Boone, 2011):

- First Generation: Rotate/Translate, Pencil Beam CT

- Second Generation: Rotate/Translate, Narrow Fan Beam CT

- Third Generation: Rotate/Rotate, Wide Fan Beam CT

- Fourth Generation: Rotate/Stationary CT

- Fifth Generation: Stationary/Stationary CT

- Sixth Generation: Helical CT

- Seventh Generation: Multiple Detector Array CT

- Eighth Generation: Duel Energy CT

Each generation has improved problems of previous generations more or less. Most remarkable are the eighth generation CT scanners that are now able to provide exquisite images with short scan time and low X-ray dosage. Nonetheless, this generation is still unable to provide good energy spectrum information. Thus, the ninth generation (coming soon), which is called *spectrum CT* or *photon counting CT*, is the current research hotspot. Literally, *photon counting CT* could count the number of X-ray photons which are detected and take advantage of the energy information to provide better tomographic images.

1.3.2   X-ray Detector Development

The detector in CT is the component that captures the radiation attenuated by objects, converts the energy information into electric signals and outputs them. Different kinds of materials can be used as energy transforming units in detectors, and based on the material, there are three types of detectors.

Gas-Filled Detectors

Most of the gas-filled detectors are ionization detectors, which collect ionization induced currents in response to radiation. A voltage difference is applied to two electrodes, anode and cathode, which could be two parallel plates, a pair of wires or concentric cylinders, and gas is filled between these electrodes. Usually, there is no current flowing between electrodes because the gas is insulating without any radiation exposure. However, X-rays cause ionization to pass through the gas and the charged particles are then attracted to the corresponding electrodes. Due to low stopping power and poor absorption efficiency for X-rays, this kind of detector is not the best choice for a nuclear medical detector.

Scintillation Detectors

The scintillator is a material that can convert radiation energy into visible light. The amount of visible light emitted after the interaction is always proportional to the energy deposited by the incident photon in a particular scintillator. Thus measuring the amount of visible light captured, then converting it into an electric signal, indicates the energy deposited into the detector. A photoelectric converter, usually photomultiplier tubes (PMT), is necessary for scintillation detectors to convert visible light from the scintillator into an electric signal. There are two general types of scintillator: inorganic scintillator as the solid crystal and organic scintillator as the liquid solvent. The inorganic scintillator is more likely used in nuclear medical detectors compared to organic scintillator (Cherry *et al.*, 2012). Compared to gas-filled detectors, the advantages of scintillation detectors are:

- They are denser and contain higher atomic number elements (i.e. high Z nuclei), meaning better stopping power and absorption efficiency.

- Increased efficiency to generate electric signals as a part of detectors.

- Can be grown large enough to make a detector.

However, scintillation detectors have some disadvantages in practice:

- Some scintillators are fragile and have to be treated very carefully with mechanical and thermal stresses as little as possible.

- Some scintillators are highly hygroscopic and result in deterioration (usually colour change and reduced visible light emission) upon exposure to humidity.

Semiconductor Detectors

Semiconductor detectors are also ionization detectors, similar to gas-filled detectors, but with solid-state architecture. The workflow of a semiconductor detector is 1) an incoming radiation photon deposits energy E inside the semiconductor detector and generates a quantity of charge q, 2) the corresponding electrode generates signal s with charge q, 3) the detector outputs the signal s. There are certain relationships between E, q and s, thus E are assessed with s.

In CT application, the process can be understood as an incoming X-ray photon depositing its energy into the detector due to *photoelectric effect*, *Compton scattering* and *electron ionization*. Then an amount of hole-electron pairs are generated and attracted by a cathode and anode due to the built-in electric field with the detector, some charge induced on electrodes and outputted as a signal representing the original incoming X-ray.

Normally, the semiconductor is a poor electrical conductor, but the charged particles can be collected by electrodes when the semiconductor is ionized as Figure 1.10.

Silicon (Si) and germanium (Ge) are the most common materials used in the synthesis of semiconductor detectors. Cadmium telluride (CdTe) and cadmium zinc telluride (CZT) are also used. CdTe would transform into CZT, if some Cd atoms, usually $10\% \sim 20\%$, were replaced by Zn atoms. They have very similar properties.
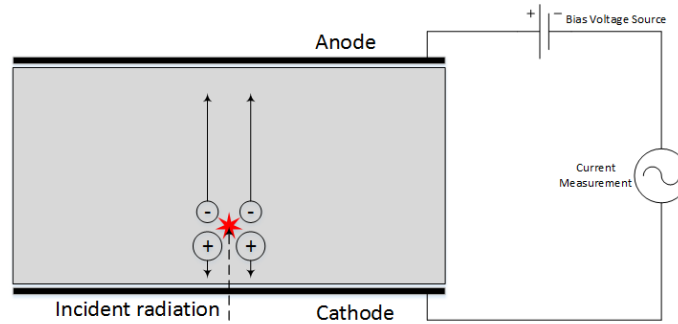
Figure 1.10: A number of hole-electron pairs are generated due to interactions between X-rays and semiconductor material. These are attracted by the cathode and the anode respectively because of the built-in electric field of the bias voltage applied between the electrodes. The output signal could be used to assess the original incoming X-ray.

Some properties of these semiconductors are listed in Table 1.2. Comparing gas-filled detectors, semiconductor detectors have much better stopping power and absorption efficiency due to higher densities and atomic numbers. Furthermore, they have better sensitivity to radiation because of lower average energy expended, which leads to better energy resolution (Cherry *et al.*, 2012).

Table 1.2: Semiconductor properties, including density, atomic number and average energy expended per ionization, including Si, Ge and CdTe, comparing to air. The data was extracted from (Cherry *et al.*, 2012).

	ρ (g/cm^3) [1]	Z [2]	W (eV) [3]
Si	2.33	14	3.6
Ge	5.32	32	2.9
CdTe	6.06	~ 50	4.43
Air	1.297×10^{-3}	~ 7.6	33.7

Furthermore, due to such high sensitivities, semiconductors can count the number of

---

[1] Density

[2] Atomic Number

[3] Average energy expended per electron-hole pair created or per ionization

photons and illustrate the radiation spectrum, meaning semiconductor detectors could provide multi-energy information with just one scan (a huge diagnostic benefit without an increase in ionizing radiation dose).

CdTe and CZT are usually used as the semiconductor materials for small nuclear medical counting and imaging detectors. Comparing to Si and Ge, CdTe and CZT have some advantages for nuclear medical imaging detectors: 1) they can work at room temperature without unbearable electronic noise, and 2) they have even higher densities and atomic numbers to block radiation more efficiently (Cherry *et al.*, 2012).

1.4   CZT Detector

1.4.1   Characters of CZT Crystal

Bonding Energy

For the interactions between radiation photons and elements, the mass attenuation coefficient of *photoelectric effect* τ is positively correlated with Z^3/E^3, while that of *Compton scattering* σ is almost invariant with both Z and E, (Cherry *et al.*, 2012), where Z is the atomic number and E is photon energy.

The *photoelectric effect* is the dominant interaction with X-ray energy range between 10 keV to 140 keV. However, the mass attenuation coefficient τ always increases suddenly at energies as orbital electron binding energies of interacted atoms. This is because the incident energy has to exceed the binding energy of specific atomic shell to trigger the *photoelectric effect*. These abrupt increases are also known as *K absorption edge* when it is related to *K-shell*, and *L absorption edge* when it is related to *L-shell* and so on.

Table 1.3 shows the bonding energies of *K-shell* and *L-shell* within Zn, Cd and Te atoms, as well as the *characteristic X-rays* that could be emitted between the *K-shell* and *L-shell*.

Table 1.3: X-ray absorption edge and energies of *characteristic X-rays* with *K-shell* and *L-shell* of Zn, Cd, and Te. The data was extracted from (Krause, 1979).

Elements	K *edge*	L$_I$ *edge*	L$_{II}$ *edge*	L$_{III}$ *edge*	KL$_{II}$	KL$_{III}$
Zn	9.673 [1]	1.208	1.057	1.034	8.639	8.616
Cd	26.727	4.034	3.742	3.554	23.173	22.985
Te	31.817	4.942	4.616	4.345	27.472	27.201

Proportion of *Photoelectric Effect* in CZT

In CZT crystals, about 80 % of the *photoelectric effect* occurs at the *K-shell* of Cd and Te atoms (Knoll, 2010), in which approximately 87% yields *characteristic X-ray* and the rest yield *Auger electrons* (Krause, 1979). Furthermore, 20 % of the *photoelectric effect* occurs at the *L-shell* of Cd and Te atoms (Knoll, 2010), in which about 7% yields *characteristic X-ray* and the rest of them yield *Auger electrons* (Krause, 1979). Thus, approximately 70 % of all *photoelectric effect* results in *K-shell characteristic X-ray*s in the CZT crystal (Shikhaliev *et al.*, 2009).

1.4.2   Structure of CZT Detector

Typically, there are two kinds of classical structures of CZT detector pixels for nuclear medical imaging applications: square pixel arrays and strip anodes arrays. The CZT detector with square pixel arrays, also known as pixelated CZT detector, is investigated in this project to utilize the position sensitivity of the detector. In Figure 1.11, the left figure shows one of its pixels with the grey square indicating the anode, the cube representing the CZT crystal and the dash-line the central line of the pixel, while the right figure shows the pixel array.

---

[1]The unit of energy is *keV* in Table 1.3.
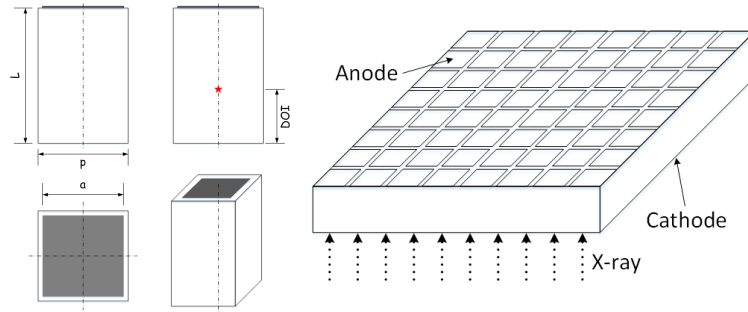
Figure 1.11: Schematic representation of square pixel. Left: Single pixel, the grey square indicates anode, the cube represents CZT crystal and the dash line represents the central line of the pixel; Right: pixels array.

To define a square pixel, the parameters, including the pitch/pixel size p, the anode size a and the thickness L, are required, and the gap between anodes of neighboring pixels is $g = p - a$. Because all the X-ray photons irradiate the cathode vertically, the depth of interaction (DOI) is the distance between the position of interaction inside the detector and the cathode. The intact square pixel CZT detector is an array of such pixels, shown at the right in Figure 1.11.

1.4.3   Types of Energy Absorption

Behavior of Photons

Since CZT has a better stopping power and absorption efficiency for X-rays, compared to other semiconductors like Si or Ge, more X-ray photons are able to be detected and absorbed with CZT detectors. However, it could be observed that some photons still escape from the pixel detector, especially if the detector is not thick enough or if the interaction is taking place close to the fringe area. Generally, there are six mechanisms of radiation absorption after interactions between incident photons and the CZT material (Figure 1.12).

1. Side escape
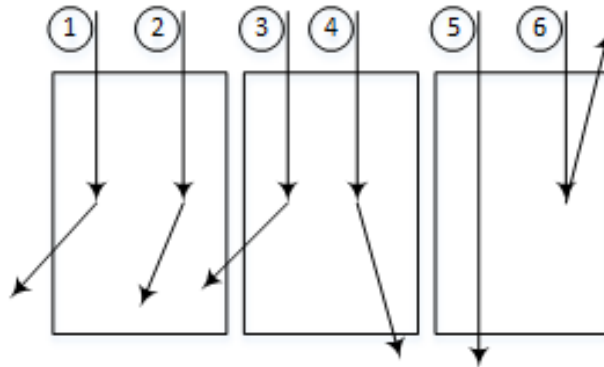
Figure 1.12: Schematic representation of six interaction mechanisms: 1) side escape; 2) full absorption; 3) cross talk; 4) forward escape; 5) penetrating and 6) back escape.

Part of the energy escapes the whole detector from the flank. This means this part of the energy is lost absolutely.

2. Full absorption

   No matter how many often interactions between incident photons or secondary particles and the CZT material occur, all of its energy is captured by the pixel hit, by the incident photon, the first time.

3. Cross-talking

   All of the energy of the incident photon is captured by the detector but with different pixels. This means the incident photon is counted more than once, and more than one anode would output the signal, each of them being smaller than the whole signal.

4. Forward escape

   Part of the energy is deposited into the detector, but the other part escapes from the front.

5. Penetrating

   The incident photon is not detected and passes through the detector without any energy loss.

6. Back Escape

   Part of the energy is absorbed, while another part is reflected back out of the detector.

Behaviour of Charge Carrier

Unlike photons, the electron can not travel long inside CZT material, or through holes. They also can lead to some effects with energy absorption.

- Charge sharing effect

  In fact, it is always in the form of electron cloud diffusion, where electrons are released from the interaction of radiation with CZT, around the position that interaction took place. With a certain diameter of the electron cloud, the charge might be collected by more than one anode, as shown in Figure 1.13 as event 2 and 3, which is called *charge sharing effect*.
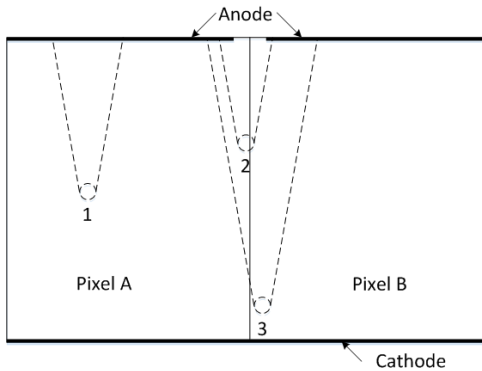
Figure 1.13: Schematic representation of *charge sharing effect*, which is the effect that the charge generated by the interaction is collected by more than one anode and yield more than one output signal, as the event 2) and 3) shown.

  The electron cloud diffusion will be expanded as it moves towards the anode, so the interaction with smaller DOI is more likely to cause a *charge sharing effect* with the larger electron cloud (dAillon *et al.*, 2006). Charge sharing effects would generate

more than one output on anodes, which means energy is lost from the original anode, resulting in deterioration of the energy resolution.

- Trapping

  Due to defects in the detector material, charge carriers might be trapped inside the detector and are subsequently not collected by the electrode. This is called trapping and brings energy loss as well as a decrease in the energy resolution (Knoll, 2010).

- Incomplete charge collection

  Holes have such poor mobility within CZT crystals that not all of them can be collected if the charge collection time is limited. Furthermore, sometimes electrons fall into the gap between anodes and are not collected by electrodes. They are called incomplete charge collections, which cause energy loss and worsens the energy resolution as well.

1.4.4　Spatial Resolution of CT Detectors

Better detectors are always able to provide more detailed information about radiation and help to reconstruct better tomographic images. The spatial resolution, which refers to the ability of the imaging modality to differentiate two objects, is one of three basic characteristics to assess the performance of CT detectors. In other words, the spatial resolution of a CT detector refers to the ability to provide sharpness or detail in geometry. Since spatial information is used to evaluate the location and the size of lesions, more information or higher spatial resolution is always helpful. Basically, the spatial resolution of a digital image from a medical imaging system is affected by two factors: 1) the resolution of the imaging device itself, including collimator resolution, intrinsic resolution, and display system or image recording device and 2) the pixel size representing the digital image (Cherry *et al.*, 2012). For example, the more pixels in a fixed field of view (FOV), the bigger the

matrix size of pixels, or the smaller the pixel size, all can deliver more image information via better spatial resolution.

Collimator Resolution

The spatial resolution of an entire imaging system is impacted by each individual part of the system. The performance of the collimator is one of the key components. Usually, the collimator between the source and the detector blocks scattered X-ray from reaching the detector. The shape, length, and diameter of the hole on the collimator affect performance metrics such as resolution and efficiency.
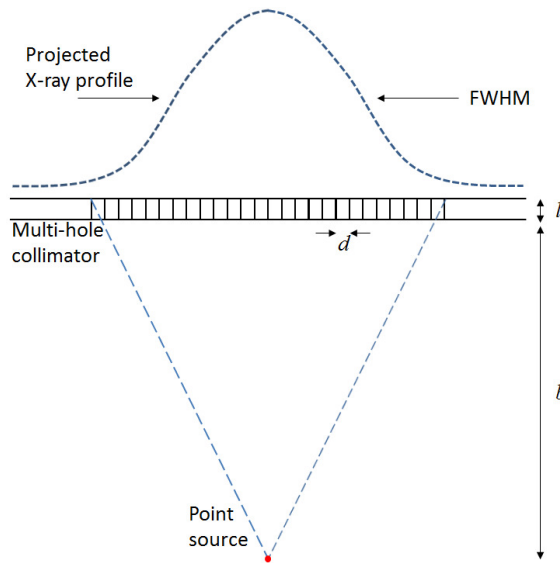
Figure 1.14: Schematic representation of the radiation profile for a parallel-hole collimator. The full width at half maximum (FWHM) of the profile is used to characterize collimator resolution. The figure is reproduced based on (Cherry *et al.*, 2012).

Collimator resolution R_{coll} is defined as the full width at half maximum (FWHM) of the X-ray profile from an X-ray point source projected by the collimator onto the detector

as Equation 1.10 (Cherry *et al.*, 2012).

$$R_{coll} \approx \frac{d(l_{eff} + b)}{l_{eff}} \tag{1.10}$$

where b is the distance between the X-ray source and the collimator, d is the diameter of the hole on the collimator and $l_{eff} = l - 2/\mu$. Here, l is the thickness of the collimator and μ is the linear attenuation coefficient of the collimator material.

The X-ray profile used in the definition of collimator resolution is also called the point-spread function (PSF), shown in Figure 1.14.

Pixel Size

Generally, small pixels bring better spatial resolution. However, with resolution limitations of the imaging device itself, there is a certain point beyond which no improvement will be gained through having smaller pixels. Furthermore, it is well understood that the signal-to-noise ratio (SNR) of an image is directly proportional to image resolution (i.e. pixel size). So, small pixels mean reduced SNR, which could lead to poor image quality, even though the resolution is 'better'. In fact, to avoid losing any imaging information with acquisition, the pixel size p must not be greater than the inverse of twice the maximum spatial frequency, which is the maximum number of distance cycles within unit length,

$$p \leqslant \frac{1}{2 \times k_{max}} \tag{1.11}$$

where k_{max} is the maximum spatial frequency (Cherry *et al.*, 2012).

Moreover, if the spatial resolution of the imaging detector is specified in terms of the full width at half-maximum (FWHM) of a line spread function (LSF), the pixel size p must

not be greater than one-third of it (Cherry *et al.*, 2012).

$$p \leqslant \frac{FWHM}{3} \qquad (1.12)$$

For example, the detector with pixel size $p = 0.5\ mm$ can not provide the $FWHM$ of LSF better than $0.5 \times 3 = 1.5\ mm$.

Modulation Transfer Function

Sometimes, PSF/LSF is insufficient for indicating spatial resolution, due to the same FWHM from PSFs or LSFs of different shapes. But the modulation transfer function (MTF), which is the imaging analog of the frequency response curve used for evaluating medical imaging instruments, can provide the most detailed specification of spatial resolution.

Considering the scale of the activity distribution varies with distance, in other words, cycles per unit length, which is called the spatial frequency and customarily symbolized by k, the ratio of the output to the input contrast is defined as MTF,

$$M_{in} = \frac{I_{max} - I_{min}}{I_{max} + I_{min}} \qquad (1.13)$$

$$M_{out} = \frac{O_{max} - O_{min}}{O_{max} + O_{min}} \qquad (1.14)$$

$$\mathrm{MTF_k} = \frac{M_{out}(k)}{M_{in}(k)} \qquad (1.15)$$

where k is the spatial frequency, I_{max} and I_{min} are the maximum and minimum radiation intensities emitted and O_{max} and O_{min} are the maximum and minimum image intensities emitted. M_{in} is the input contrast and measured in terms of object radioactivity or emission rate and M_{out} is the output contrast measured in terms of counting rate, image intensity and so on.

M_{out} ranges from 0, when there is no contrast at all or $O_{max} = O_{min}$, to unity, when

the contrast is the most or $O_{min} = 0$. Since the output contrast M_{out} and the MTF are positively correlated, larger output contrast M_{out} is indicative of better image resolution.

With MTF, any image could be described as a summation of sine waves of different frequencies. An imaging system with a flat MTF curve whose value is close to unity produces the most faithfully reproduced image based on the imaged object.

1.5   Motivation

As everyone knows, cancer is one of the greatest enemies of mankind and became a major public health problem all over the world.

In the United States, an estimated $1,685,210$ new cases of all cancers combined and $595,650$ deaths from all cancers combined would occur in 2016. The incidence and mortality rates for all cancers combined are 454.8 and 171.2 per $100,000$ people respectively. About 39.6% of Americans are expected to be diagnosed with cancer in their lifetime. Furthermore, there were 14 million Americans living with cancer in 2014 and it is expected to rise to almost 19 million by 2024 (NCI, 2016).

In China, cancer is the leading cause of death with increasing incidence and mortality. Around $4,292,000$ new cases of all cancers combined and $2,814,000$ deaths from all cancers combined occurred in 2015. The incidence and mortality rates for all cancers combined are 213.6 and 149.0 per $100,000$ Chinese people respectively per year in rural areas due to the significantly higher rate for senior residents. Meanwhile, there are 191.5 and 109.5 per $100,000$ Chinese people respectively in the urban area who developed cancer in 2015 (Chen *et al.*, 2016).

In Canada, cancer is responsible for 30.2% of all deaths and hence is a highly significant health problem. An estimated $202,400$ new cases of all cancers combined and $78,800$ deaths from all cancers combined would occur in 2016. About 2 in 5 Canadians is expected to

develop cancer in their lifetime and 1 in 4 will die of it. And there were $810,000$ Canadians living with cancer which had been diagnosed in the previous 10 years at the beginning of 2009 (CCS, 2016).

In detail, lung cancer is the most common cancer all over the world and as such is the leading cause of more than 1.3 million estimated deaths annually worldwide (Center *et al.*, 2011). In the United States, lung and bronchus cancer brought $224,390$ cases, 13.32% of all kinds of cancer cases, and $158,080$ deaths, 26.67% of all kinds of cancer deaths, in 2015 (Siegel *et al.*, 2016). In China, lung cancer contributes approximately 17% of all cancer cases, due to awful air pollution and large cigarette smoking population (Siegel *et al.*, 2016). In Canada, about 1 in 12 men and 1 in 15 Women are expected to develop lung cancer during his/her lifetime, while 1 in 13 and 1 in 17 will die from it correspondingly. Lung cancer contributes 14% of all new cancer cases and 27% of all cancer deaths in 2015 (Chadder *et al.*, 2016). Furthermore, the 2-year age-standardized relative survival ratio (ARSR) of stage I lung cancer ranges from 66.5% in Prince Edward Island to 84.8% in Ontario, while 2-year ARSR of stage IV lung cancer ranges from 7.6% in Manitoba to 13.2% in British Columbia. These data show that significant improvement of the ARSR would be better if lung cancer could be diagnosed at an earlier stage. However, the ratio of lung cancer diagnosed in stage IV ranges from 44.8% in Ontario to 56.8% in Saskatchewan out of all lung cancer diagnosed cases (Chadder *et al.*, 2016).

Beside lung cancer, breast cancer is the most common cancer and the 2nd leading cause of death from cancer in women. Unlike lung cancer, breast cancer has an extremely high incidence in women, although its mortality is relatively lower. In the United States, $246,660$ women will be diagnosed with breast cancer, which is 14.6% of all new cancer cases in women, while $40,450$ women will die from breast cancer, in 2016. During their lifetime, about 12.4% American women will be diagnosed with breast cancer. In Canada, $25,700$ women will be diagnosed with breast cancer, which is 26% of all new cancer cases in women,

while 4,900 women will die from breast cancer, which is 13% of all cancer deaths in women, in 2016. During their lifetime, about 1 in 9 Canadian women are expected to develop breast cancer.

Plenty of work has been done on CZT detectors for breast CT scanning (GLICK and DIDIER, 2011; Shikhaliev and Fritz, 2011; Kalluri *et al.*, 2011; Ding *et al.*, 2012; Kalluri *et al.*, 2013; Makeev *et al.*, 2013; Glick, 2014). CT would have advantages over mammography as mammograms are 2D projections through the breast. Thus CT could be an important method of annual screening for breast cancer (if the dose could be reduced). On the other hand, according to the National Lung Screening Trial (NLST), compared to other methods, including chest radiography, low-dose CT (LDCT) results in a 20% reduction in lung cancer-specific mortality (Aberle D., 2011). In other words, LDCT scan is an effective method to benefit patients from lung cancer mortality. However, LDCT is still a highly controversial issue because of large dose accumulation by annual screening, due to the low utilization of radiation with the intrinsic problem of conventional CT detector, not to mention more than one scan is indispensable sometimes for lung cancer monitoring during the critical period. Fortunately, the novel spectrum CT with photon counting detector, such as CZT detector, is a potential solution for this problem, but the spatial resolution becomes another issue. For instance, in post-contrast thorax CT a sub-millimeter spatial resolution is needed. And for breast CT, required resolution is on the order of 100 μm or better (Makeev *et al.*, 2013).

Therefore, it is important and necessary to investigate CZT spatial resolution, and to thoroughly understand the physical quantities that affect it's resolution capabilities.

Chapter 2

Analysis of Interactions within CZT Material

2.1 Simulation Background

2.1.1 Weight Fraction

As mentioned in Section 1.3.2, CdTe would transform into CZT, when some Cd atoms are replaced by Zn atoms. Say if x ($x \in (0,1)$) Cd atoms were replaced by Zn atoms, CdTe becomes to $Cd_{1-x}Zn_x Te$ or $C_{1-x}Z_x T$. It could be understood as $1-x$ unit CdTe and x unit ZnTe mixed together by a crystal growing process. Since the standard atomic weights of Cd, Zn and Te are 112.41, 65.38 and 127.60 respectively, the weight fractions of Cd, Zn and Te are $W_{Cd} = 0.4299$, $W_{Zn} = 0.0278$ and $W_{Te} = 0.5423$ proportionately, in $Cd_{1-x}Zn_x Te$ when $x = 0.1$. All the data with CZT used in this thesis are simulated with $Cd_{0.9}Zn_{0.1}Te$ material.

2.1.2   X-ray Point Source

In this thesis, a 1 μm radius X-ray point source is used for all simulations, located on the central line of the CZT crystal pixel and 10 cm away from the edge. The X-ray point source emits X-ray photons within $\theta = 0$ and $\phi \in [0, 2\pi)$ with energy from 10 keV to 140 keV, which means the X-ray photon flow move towards the CZT crystal directly with the direction vertical to the electrode plane. There is no collimator between the point source and the detector in the simulation. According to Section 1.4.4, the point-spread-function here is a pulse with width $w = 2$ μm, and the distance between the point source and the detector has nothing to do with the spatial resolution at all. In some simulations and experiments, only one-dimension is discussed for simplicity, and the point-spread-function would be regarded as line-spread-function (LSF).

2.1.3   Monte Carlo Method

The Monte Carlo (MC) method, named after an administrative area of the Principality of Monaco, is a class of computational algorithms that approaches an optimum result more accurately with increasing numbers of repeated random samplings. Its basic idea is solving problems that might be deterministic in principle, but with the concept of randomness. Monte Carlo methods are frequently used for optimization, numerical integration, and probability distribution. In nuclear medical equipment research, the Monte Carlo method is often used in the simulation of movement of radioactive particles, such as GEometry ANd Tracking (GEANT4) for high energy physics (Allison *et al.*, 2006) and Application to Tomographic Emission (GATE) for a modular, versatile, scripted simulation for medical imaging device designs (Jan *et al.*, 2004). For this thesis all data concerning X-ray photons, electrons and all their interactions, was simulated with GATE. For each event, the coordinates, time, energy deposited into semiconductor and type of effect are saved in list mode files.

2.2   Interactions with CZT Detector

2.2.1   Profiles of Full Absorption

According to Section 1.4.1, the dominant X-ray interaction occurs through the *photoelectric effect* in the energy range of $10 \sim 140\ keV$. To investigate the interactions with radiation inside the CZT crystal using GATE, a series of $1\ \mu m$ radius X-ray sources each yielding a monochromatic X-ray beam (energy range from $10 \sim 140\ keV$ at $5\ keV$ increments) was tested. For each increment in photon energy photons struck the same point on the surface of a large enough CZT crystal to make sure no energy of those X-rays could escape from it.

According to *Lambert-Beer's Law*, Equation 1.1, the attenuation of a monochromatic X-ray passing through a homogeneous object obeys an exponential decay. Figure 2.1 shows profiles of photon numbers with different energies fully absorbed inside of CZT crystal.
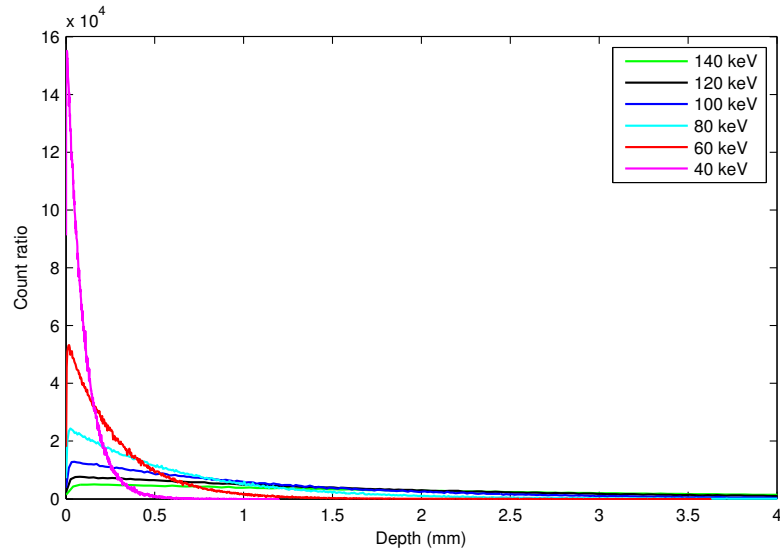

Figure 2.1: Profiles of photon numbers with different energies fully absorbed, which is an exponential decay with the depth of interaction following the *Lambert-Beer's Law*. The photon with high energy could dive deeper into the CZT crystal. At the same depth, the proportion of fully absorbed events is bigger with lower energy photons than higher energy photons.

Obviously, the higher energy photons penetrate deeper into the crystal, eventuallyleads to 100% absorption. At the same time higher the peak count rate goes deeper as the energy increases. Table 2.1 provides the full absorption percentages with different depths and different energies.

Absorption proportion decreases monotonically as radiation energy increases. For the X-ray with energy 120 keV, 79.61% of all the photons are fully absorbed within 3 mm depth and 88.15% within 4 mm depth. It means the thickness of CZT crystal has to be 4 mm at least to be efficient enough dealing with 120 keV X-ray.

Table 2.1: Full absorption percentage with depth and energy. With the lower energy photons, the full absorption depth is smaller and the absorption percentage is bigger at the same depth, comparing to the higher energy photons. For the depth $d = 3\ mm$, 100.00% of X-ray photons with energy 60 keV could be full absorbed, while it is 79.61% with 120 keV X-ray photons.

	40 (keV)	60 (keV)	80 (keV)	100 (keV)	120 (keV)	140 (keV)
1 mm	100.00%	97.13%	79.66%	57.50%	40.27%	28.59%
2 mm	100.00%	99.92%	95.98%	82.30%	65.04%	49.94%
3 mm	100.00%	100.00%	99.21%	92.70%	79.61%	65.04%
4 mm	100.00%	100.00%	99.84%	96.98%	88.15%	75.68%
5 mm	100.00%	100.00%	99.97%	98.76%	93.12%	83.06%
6 mm	100.00%	100.00%	99.99%	99.49%	96.02%	88.23%
7 mm	100.00%	100.00%	100.00%	99.79%	97.70%	91.85%

Table 2.1 provides the average depth of full absorption with different energies. For the X-ray with energy 60 keV, the average depth of the full absorption is 286.2 μm, while it is 1910.6 μm with 120 keV X-ray. X-rays with energy 50 keV to 60 keV are used for breast cancer scanning with breast CT (Makeev *et al.*, 2013), while 120 keV is used for lung cancer scanning with LDCT (Aberle *et al.*, 2001). Therefore, DOI = 0.3 mm and DOI = 1.8 mm, which represent the average depth of full absorption of X-rays with energy 60 keV and 120 keV respectively, were used for simulations in this thesis.

Table 2.2: The average depth of full absorption with different energies. For the X-ray with energy 60 keV, the average depth of full absorption is 286.2 μm, while it is 1910.6 μm with 120 keV X-ray.

Energy (keV)	40	60	80	100	120	140
Depth (μm)	95.6	286.2	633.6	1168.4	1910.6	2866.5

2.2.2 Proportions of Different Interactions

To evaluate the proportions of different interactions in detail, simulations were performed under two conditions: first with a 4.0 mm thick CZT detector fixed and a variety of incident photon energies, and second, using only 60 keV and 120 keV X-ray photons with a variety of detector thicknesses.

Radiation Energy Variations

Considering all the interactions inside a 4.0 mm thick CZT detector, the proportion of normalized *photoelectric effect*, *Compton scattering* and *Rayleigh scattering*, in cross section, are shown in Figure 2.2. At an average X-ray energy of 60 keV, the fraction of *photoelectric effect*, *Compton scattering*, and *Rayleigh scattering* are 94.58%, 1.69% and 3.74% respectfully, while they are 82.72%, 9.87% and 7.41% respectively, at the higher X-ray energy of 120 keV.

A trough is found on the *photoelectric effect* curve at 25 keV because it is just less than the *K-shell* X-ray absorption edges of both Cd and Te atoms (Table 1.3). In other words, these X-ray photons are too weak to trigger *photoelectric effect*s on those atoms. Similarly, X-rays with 30 keV energy would cause *photoelectric effect*s with Cd atoms but not Te atoms. Thus, the proportion of *photoelectric effect* at 30 keV is a little bit higher than 25 keV. Although the amount of *photoelectric effect* keeps decreasing while *Compton scattering* and *Rayleigh scattering* increase with X-ray energy, at less than 40 keV the *photoelectric effect* is the dominant interaction.
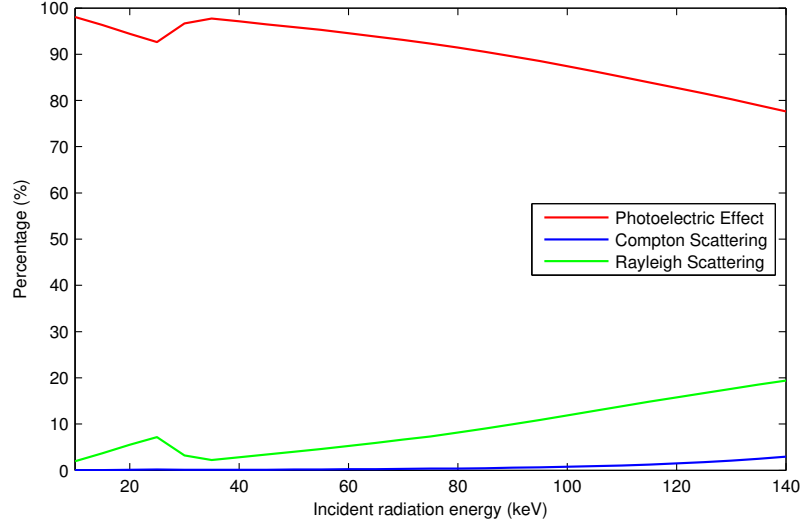
Figure 2.2: Percentage of three kinds of interactions, including *photoelectric effect*, *Compton scattering*, and *Rayleigh scattering*, with different energies. Generally, the proportion of *photoelectric effect* decreases as X-ray energy increases, while the proportions of *Compton scattering* and *Rayleigh scattering* increase.

Detector Thickness Variation

All interactions with X-ray photons can be put into three categories: 1) *photoelectric effect*, represented as *PE*, the interactions only contain *photoelectric effect* once, 2) *Compton scattering* only, represented as *CS*, the interactions only contain *Compton scattering* once, and 3) multiple interactions, represented as *mi*, all other interactions which contain *Compton scattering* more than once, both *Compton scattering* and *photoelectric effect* as well as other interactions with X-ray photons. Table 2.3 shows the ratios of these with different thicknesses of CZT crystal ranging from 2 *mm* to 8 *mm*.

With 120 *keV* X-rays, the proportion of interaction resulting only in *photoelectric effect* is about 82.70% and this is fairly stable with thickness, while the ratio of interaction leading only to *Compton scattering* keeps decreasing from 2.80% to 0.90% as thickness increases. For 60 *keV* X-ray, it can be proven that the ratio of interactions of *photoelectric effect*,

which is 94.55%, is independent of the thickness as well, although 97.13% and 99.92% of all the photons are fully absorbed within 1 mm and 2 mm respectively according to Table 2.1.

Table 2.3: Ratio of three kinds of interactions, including *photoelectric effect* (PE), *Compton scattering* (CS), and multi-interactions (MI), at different depths with 60 keV and 120 keV X-ray. Generally, the percentage of interactions does not change as the depth changes when the energy of the X-ray photon is fixed.

	PE^1	CS^1	MI^1	Ratio[1] [3]	PE^2	CS^2	MI^2	Ratio[2] [3]
2 mm	94.55%	0.21%	5.24%	18.08	82.67%	2.80%	14.53%	5.88
3 mm	94.55%	0.21%	5.24%	18.07	82.70%	1.95%	15.35%	5.51
4 mm	94.55%	0.21%	5.24%	18.07	82.72%	1.49%	15.79%	5.33
5 mm	94.55%	0.21%	5.24%	18.07	82.71%	1.22%	16.07%	5.22
6 mm	94.55%	0.21%	5.24%	18.07	82.70%	1.06%	16.24%	5.16

2.2.3   Distribution of Different Interactions

Figure 2.3 shows the full absorption spatial distribution on the *X-Y plane* of interactions of *photoelectric effect* (PE only), *Compton scattering* (CS only) and multiple scatterings (MI) within a CZT crystal, with radius 1 μm around the X-ray source with both 60 keV and 120 keV energies.

Obviously, the end positions of interactions of *Compton scattering* only gather primarily around the hitting point of the source, and *photoelectric effect* scatters a little more than *Compton scattering*, while multiple scattering spreads the furthest.

---

[1]60 keV X-ray

[2]120 keV X-ray

[3]Ratio between signal interaction and multi-interactions
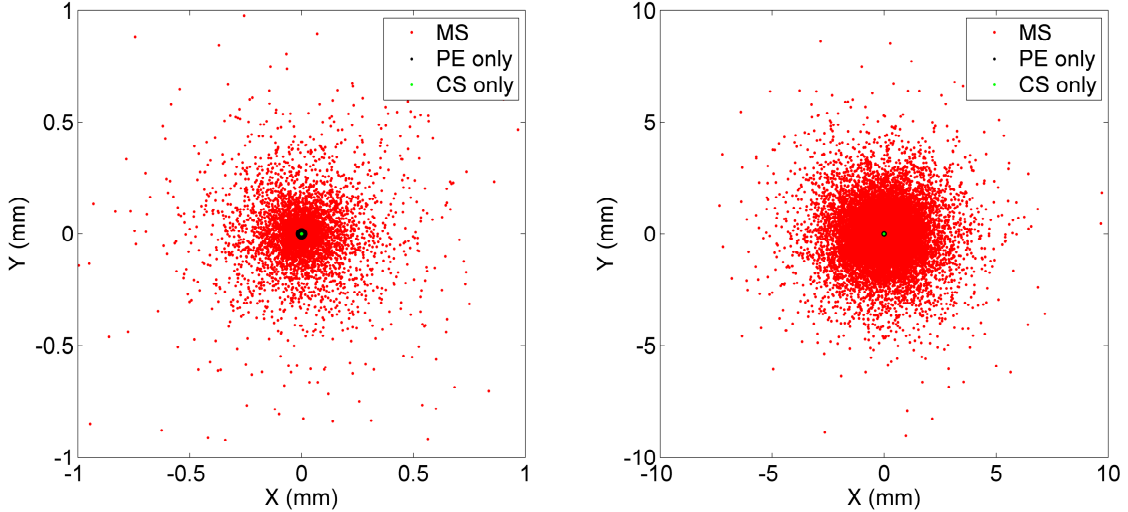
Figure 2.3: Distribution of end positions of interactions: including *photoelectric effect* (PE only), *Compton scattering* (CS only), and multiple scatterings (MS), with 60 *keV* (the left figure) and 120 *keV* X-ray (the right figure). Higher energy X-ray spreads its energy further.

Distribution of *photoelectric effect* Only

The *photoelectric effect* would occur on different shells of different atoms with different proportions (Section 1.4.1). The ratios of nine kinds of *photoelectric effect*s with different energy radiations are shown in Figure 2.4. With incident radiation energy higher than 50 *keV* until 140 *keV*, the ratios are relatively stable. Approximately, 51% of *photoelectric effect*s occur on *K-shell* of Te atoms, and 34% on *K-shell* of Cd atoms, which are the two dominant types, while the other kinds of *photoelectric effect*s are no more than 5% each.

The distance a photoelectron travels within the CZT material is related to its kinetic energy, which is the difference between the original energy of the incident photon and the energy deposited into the CZT detector during the *photoelectric effect*. Since the *photoelectric effect* on the *K-shell* of Te, Cd and Zn atoms are the top three possibilities, three rings of end positions of ejected photoelectrons could be observed in Figure 2.5, corresponding to
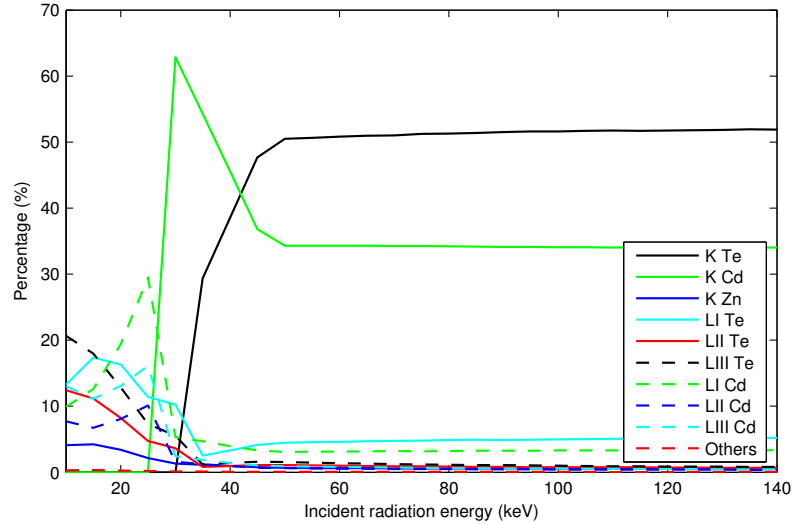
Figure 2.4: Percentage of the *photoelectric effect* on different shells of different atoms with different energies. Most of the *photoelectric effect* is on the *K-shell* of Te atom and the *K-shell* of Cd atom, whose percentage is stable when the energy of X-ray is higher than 50 *keV*.

three levels of photoelectron kinetic energies. Photoelectrons from the *K-shell* of Zn atoms have the most kinetic energy among these three kinds of photoelectrons and distribute furthest from the original hitting spot, but no more than 20 *μm* with 60 *keV* X-ray, shown in the left figure, and 60 *μm* with 120 *keV* X-ray, shown in the right figure. Comparing 60 *keV* to 120 *keV* X-rays the latter spreads its energy further.

Other photoelectrons with higher kinetic energies can be ignored due to a low proportion of these with respect to the total of other photons. The situation is more complicated when the incident radiation energy is lower than 45%, because of the energy thresholds for the *photoelectric effect*s on *K-shell*s of Cd and Te atoms. However, their photoelectrons have lower kinetic energies and run through closer due to lower original incident radiation energy. Therefore, the interactions of *photoelectric effect* only are unlikely to cause side escape or cross talk between detectors.
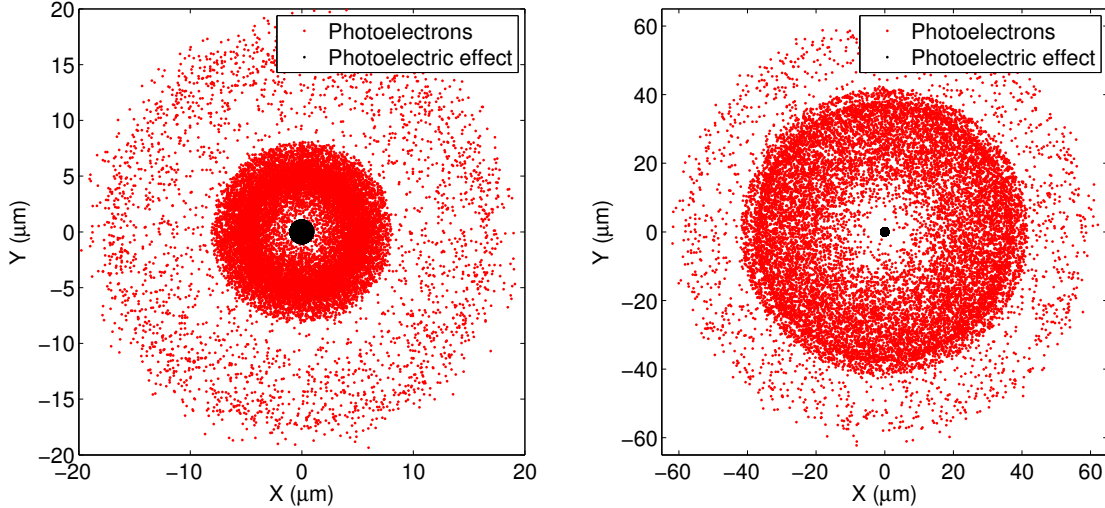
Figure 2.5: distribution of *photoelectric effect* only with 60 *keV* X-ray (left) and 120 *keV* X-ray (right). The three rings of end positions of ejected photoelectrons indicate the *photoelectric effect* on the *K-shell* of Te atom, Cd atom and Zn atom respectively.

Distribution of *Compton scattering* Only

Considering all the photons from *Compton scattering*, the average energies deposited into the CZT crystal is quite low compared to the original X-ray photons as shown in Figure 2.6. In fact, the average energies deposited into the CZT detector, which lead to comparable energies of recoil electrons, are about 1% of the energies of the incident radiation. According to Equation 1.8 and Equation 1.9, small E_{re} means small θ and big E_{sc}. Thus, scattered photons would almost move along the original trajectory after *Compton scattering*. This has been proven and is shown in right figure of Figure 2.6.

The black dots represent the positions of all the *Compton scattering*s, forming a 1 μm radius circle. The red dots represent the end position of all the recoil electrons within the events of only *Compton scattering*, located in an area less than 5 μm in radius. Therefore, the interaction of only *Compton scattering* can rarely lead to side escape or cross-talking.

38
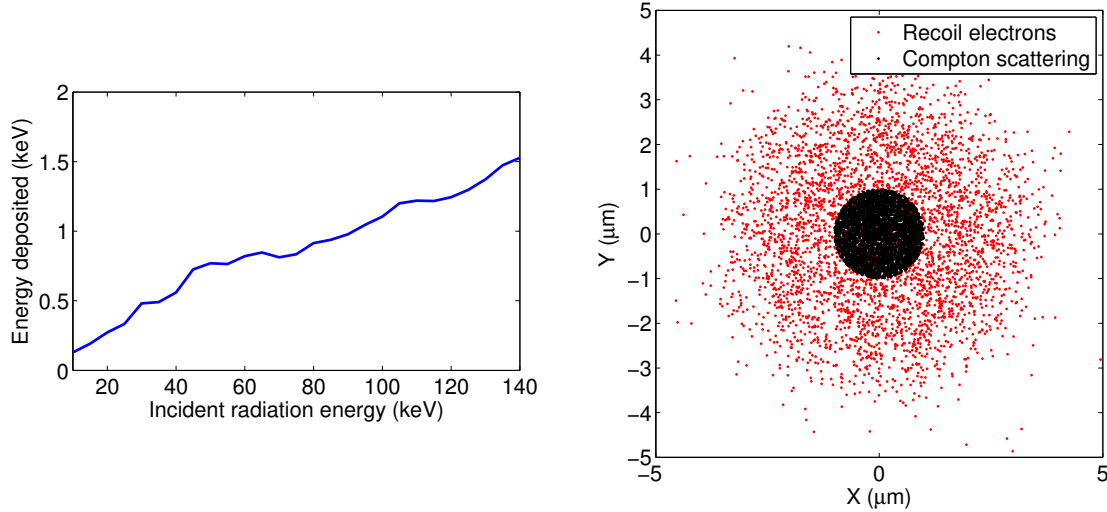
Figure 2.6: Left: average energies deposited into the CZT detector with *Compton scattering* in interaction of *Compton scattering* only; Right: Distribution of end positions of *Compton scattering*s and recoil electrons in interaction of *Compton scattering* only with 120 *keV* X-ray photon.

Distribution of Multiple Scattering

There are several kinds of interactions with multiple scattering categories, including *Compton scattering* more than once, both *Compton scattering* and *photoelectric effect* and other interactions. As previously analyzed, the interaction of *Compton scattering* more than once would not cause significant cross talk, nor would the interaction of both the *Compton scattering* and the *photoelectric effect*. However, the other interactions, which contain *Rayleigh scattering* is another story. Although *Rayleigh scattering* would not deposit any energy into CZT crystal, it significantly deflects the trajectory of the original photon.

Figure 2.7 shows the end positions of *Rayleigh scattering*s and full absorption in the interaction of multiple scatterings with 120 *keV* X-ray photons. The observed energy is scattered to a range of 2.0 *mm* for most incident photons, even occasionally up to 10.0 *mm*,
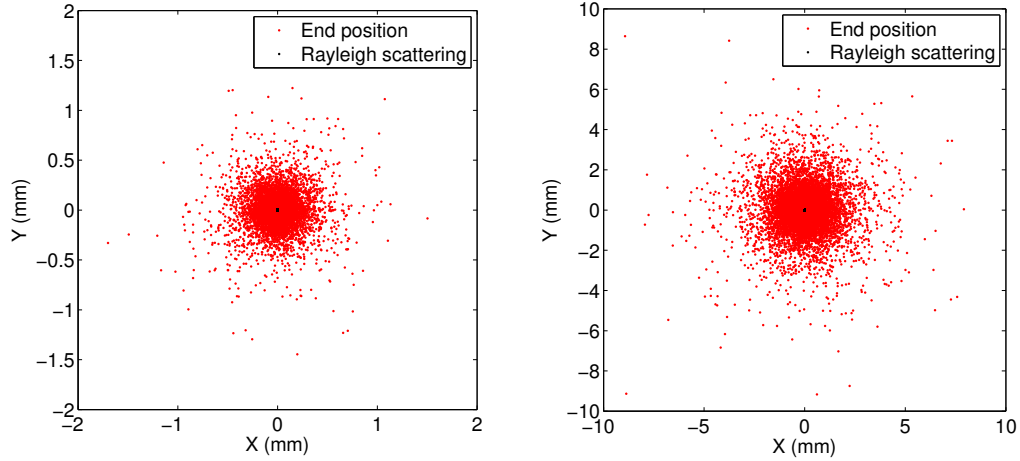
Figure 2.7: Distribution of end positions of *Rayleigh scattering*s and full absorption in interaction of multiple scattering with 60 *keV* (left) and 120 *keV* (right) X-rays.

which is much larger than the *photoelectric effect* and *Compton scattering*. This means interactions of multiple scattering bring added noise into the detector and this is unavoidable. Fortunately, the proportion of interaction of multiple scattering is rather low with X-ray energy less than 140 *keV*, for example, 7.41% at 120 *keV* (Section 2.2.2) and even smaller at 60 *keV*.

Characteristic X-Ray

Characteristic X-rays are emitted if vacancies on atomic inner shell electron get filled by electrons from outer shells. These are also known as *K-edge* characteristic X-rays, mentioned in Section 1.2.4. According to Section 2.2.2, at an average X-ray energy of 60 *keV*, the fraction of *photoelectric effect* is 94.58%, while it is 82.72%, at a higher X-ray energy of 120 *keV*. As shown in Figure 2.4, approximately, 51% of *photoelectric effect*s occur on *K-shell*s of Te atoms, and 34% on *K-shell*s of Cd atoms, with incident radiation energy higher than 50 *keV* until 140 *keV*. The proportions of *photoelectric effect* on *K-shell* of Zn atoms and on *L-shell* of all three kinds of atoms are too small to be considered here, as Figure 2.4

shows. Thus, approximately, 48.24% and 32.16% of all 60 keV X-ray photons interacts with CZT material for *photoelectric effect* and leaves vacancies on *K-shell* of Te atoms and Cd atoms respectively, while 42.19% and 28.12% with 120 keV X-ray photons. Given 87% of vacancies on *K-shell* yields characteristic X-rays and the rest of them yield *Auger electron*s approximately (Section1.4.1), 41.97% and 27.98% of total numbers of 60 keV X-ray photons would yield out *K-edge* characteristic X-rays of Te atoms and Cd atoms respectively, while 36.70% and 24.47% with 120 keV photons. Due to the very short distance that electrons with such low energy could travel inside of the CZT crystal, *Auger electron*s were not considered here.

Because the average energy of *K-edge* characteristic X-rays of Te atoms is 27.5 keV, which is higher than the *K-shell* binding energy of Cd atoms (26.73 keV) (Table 1.3), there is the possibility of a second *photoelectric effect* on the *K-shell* of Cd atoms. However, the average energy of *K-edge* characteristic X-ray of Cd atoms is 23.4 keV, which could not trigger another *photoelectric effect* on *K-shell* of Cd or Te atoms. These secondary X-ray photons could travel further than photoelectrons even with higher energies.

Figure 2.8 shows the attenuation profiles of 23.4 keV and 27.5 keV X-rays within a CZT detector. The average distance of full absorption are 130 μm and 70 μm respectfully. The
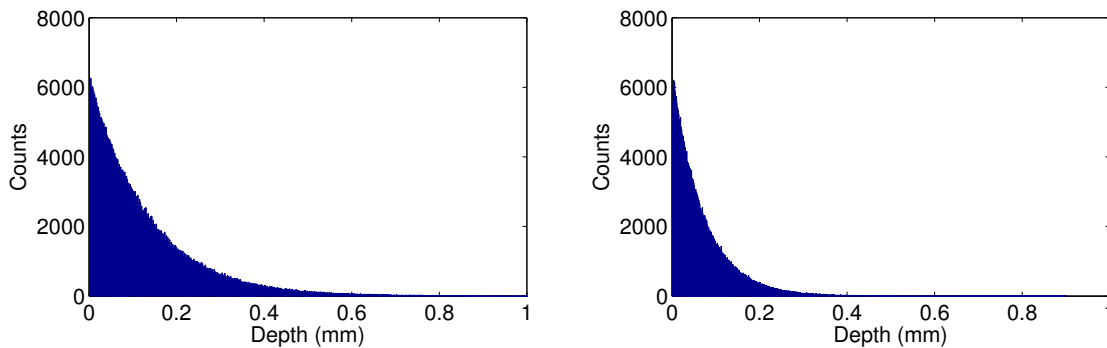

Figure 2.8: Attenuation profiles of characteristic X-ray of Cd atom (left) and Te atoms (right). The average distance of full absorption are 130 μm and 70 μm respectfully.

average depth of full absorption of Te atoms is shorter than Cd atoms, while its energy is higher. This is because part of the energy of *K-edge* characteristic X-rays from Te atoms would travel in the form of photoelectron kinetic energy, due to the second *photoelectric effect* on Cd atoms. According to Figure 2.2, about 95% of interactions are *photoelectric effect*s with 27.5 *keV* characteristic X-ray, and about 65% of X-ray photons with energy 30 *keV* would trigger *photoelectric effect*s on *K-shell* of Cd atoms (Figure 2.4). Thus, characteristic X-rays on the *K-shell* of Te and Cd atoms scatter the energy approximately 99 μm away from the original position of the interaction (on average), indicating part of the energy would be spread 70 μm away in the *X-Y Plane* on average possibly leading to side escape or cross talk effects.

2.2.4 Electron Cloud and Concentration

Photoelectrons are emitted in the *photoelectric effect* and create a distribution of electron-hole pairs due to *ionization* along its trajectory. The distribution is specifically called a cloud, where an electron cloud is a distribution of electrons. The range of a photoelectron effect depends on its energy. For instance, a 100 *keV* photoelectron stops within 47 μm but only 10 μm for a 40 *keV* photoelectron (Kalemci and Matteson, 2002).

At room temperature in CZT material, the mobility of electrons and holes are assumed to be coordinate-independent and regarded as $\mu_e = 1000 \ cm^2/Vs$ and $\mu_h = 100 \ cm^2/Vs$ respectively in this thesis, then the instantaneous velocity and the traveling time of the carriers could be represented as

$$\vec{v} \quad = \quad \mu\vec{E} = \frac{\mu V}{L} \tag{2.1}$$

$$t \quad = \quad l/\vec{v} = \frac{Ll}{\mu V} \tag{2.2}$$

where V is the bias voltage applied between anode and cathode that builds a uniform

internal electric field, l is the distance that charges traveling within CZT detector and L is the thickness of CZT detector. For the bias voltage, there is a negative potential applied to the cathode and the anodes are kept typically at 0 V. Since the hole mobility is much less than the electron and the hole could not be fully collected by electrodes within collecting time probably, the transit signals and the collecting signals cause by holes are not investigated in this thesis.

Since electrons move toward the anodes due to the constant uniform electric field created by the bias voltage, and their mobility is assumed to be constant within the CZT material, their instantaneous velocity is stable no matter where they started or where they are within the detector (Equation 2.1). Thus, their traveling times have linear correlations with the distances at which they passed through the detector. In other words, their traveling times could reflect their DOIs, given their terminal destinations are at the anode plane (Equation 2.2).

As mentioned in Section 1.4.3, the electron cloud expands its diffusion while it moves towards the anode and would thus split its energy onto more than one anode if a *charge sharing effect* occurred. Previous work (Kalemci and Matteson, 2002) claims the size of the electron cloud could be evaluated according to *Fick's equation* as a function of its DOI, the standard deviation σ at time t, and its initial electron cloud with a delta-function distribution, given by Equation 2.2 (Kalemci and Matteson, 2002)

$$D_e \quad = \quad \frac{kT\mu_e}{q} \tag{2.3}$$

$$\sigma^2 \quad = \quad 2D_e t = \frac{2kTLl}{qV} \tag{2.4}$$

where D_e is the diffusion coefficient of the electron, k is Boltzmann's constant, T is absolute temperature and q is the elementary charge (Kalemci and Matteson, 2002).

The left plot in Figure 2.9 shows the standard deviation σ changes with the DOI when
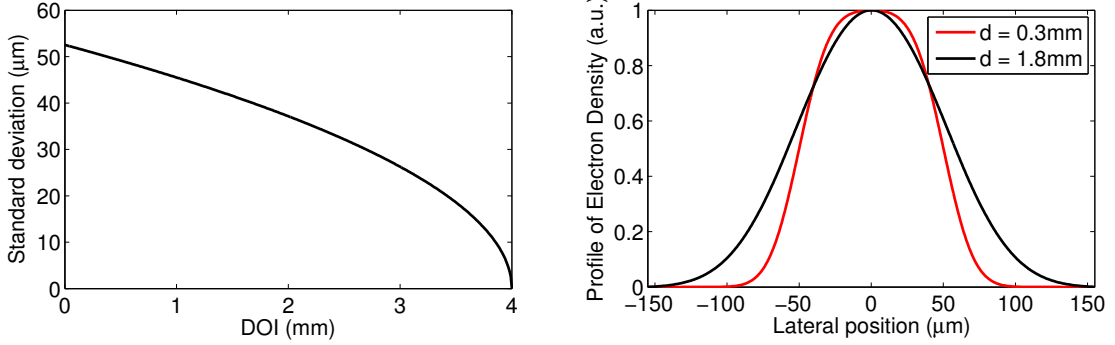
Figure 2.9: Left: The profile of standard deviation with full traveling distance; Right: The profile of electron density with different depths within the CZT detector (The bias voltage is 300 V and the thickness of detector is $L = 4\ mm$).

bias voltage is set at $V = 300\ V$. Since l is the distance that electrons travel within the CZT detector, a small DOI means bigger distance (l) travelled in the detector which results in broadening the standard deviation. The maximum standard deviation $\sigma_{max} \approx 53\ \mu m$ appears at DOI ~ 0, very close to the cathode where electrons have the longest traveling distance as well as traveling time within the CZT detector. The bias voltage also impacts the standard deviation. Basically, a higher bias voltage brings stronger internal electric field and makes faster velocity of electrons, which means less traveling time and less broadening of the standard deviation of the electron cloud.

The electron cloud radius r is estimated with FWHM approximation for the Gaussian distribution of the electron as (Iniewski *et al.*, 2007):

$$r = 1.15\sigma = 1.15\sqrt{\frac{2kTLl}{qV}} \tag{2.5}$$

Therefore, the maximum electron cloud radius $r_{max} = 1.15\sigma_{max} \approx 61\ \mu m$ at DOI ~ 0. Also, when DOI $= 0.3$ mm, $l = L - \text{DOI} = 3.7$ mm, it is easy to find out the maximum electron cloud radius $r_{max}|_{l=3.7\ mm} \approx 57\ \mu m$, which was used for simulations in this thesis.

After considering the position of photoelectrons emitted out of the radius of the electron

cloud, together with the electron numbers, an indication on the lateral distribution of electrons within the CZT detector can be determined. From Equation 2.2, it is simple to determine that the traveling time for the electron within the CZT detector is $t_e = \frac{Ll}{\mu_e V} \approx$ 500 ns for a 4 mm distance and bias voltage $V = 300$ V This is much less than its trapping time of 3 μs (Kalemci and Matteson, 2002). So the density of the electron cloud depends on the time as well as the distance the electron has traveled within the material. Thus, for a delta function initial concentration $M_0\delta(x_0, 0)$ at x_0, the one-dimensional solution for concentration $M(x, t)$ at position x and time t is represented by a Gaussian (Beam, 1965):

$$M(x, t) = \frac{M_0}{2\sqrt{\pi D t}} \; e^{\frac{-(x-x_0)^2}{4Dt}} \tag{2.6}$$

The right figure in Figure 2.9 shows the profile of electron density with different DOIs. It means a smaller DOI leads to a higher electron density, while a larger DOI spreads electrons a little bit further away.

2.3 Collecting Signal

2.3.1 Proportion of Charge Sharing Events

Within the CZT detector, *charge sharing effect* would split the energy of the incident photon into more than one component on different anodes. In fact, not only photoelectrons with higher energy cause *charge sharing effect* more easily but also the configuration of the detector affects the proportion of charge sharing events. For example, a small gap size makes electron cloud coupling between two anodes easier. Thus can also be exacerbated if the anode size is too small. After comparing the gap size of the detector, g, with the radius of the electron cloud, r, Iniewski (Iniewski *et al.*, 2007) categorized pixel arrays into two types: small gap pixels, $g < 2r$, and large gap pixels, $g \geqslant 2r$. Then a proximity region, c,
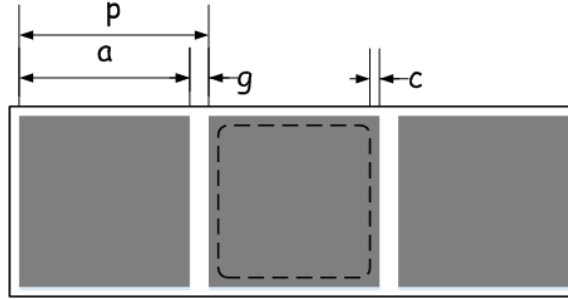
Figure 2.10: The definition of a proximity region on the anode of the pixel array. All interactions with projection within the area of c are likely to have *charge sharing effect*.

was introduced to investigate the proportion of charge sharing events, for small gap pixels, $c = g/2$, and $c = a/20$ for large gap pixels, shown in Figure 2.10.

And the proportion of charge sharing events is expressed as (Iniewski *et al.*, 2007):

$$P_{CSE} = 1 - (\frac{a + 2c - 2r}{a + g})^2 \qquad (2.7)$$

$$c = \min(g/2, a/20) \qquad (2.8)$$

2.3.2   Range of Charge Sharing Effect

The anode that collects most of the electrons is called the *collecting anode*, while the anodes adjacent to the collecting anode are called *minor-collecting anodes*. For a single event, if the collecting anode collects all the electrons and outputs full unit With the same ratio of thickness to anode size, the range of *charge sharing effect*, which is the width that is able to collect signal due to *charge sharing effect*)counting from the edge of the anode), would be influenced by the gap g, the bias voltage V and DOI. Since it has broader initial electron cloud distribution and more serious *charge sharing effect* with higher energy X-ray, the 120 keV was used for simulation in this section.

Figure 2.11 shows the range of *charge sharing effect* changing with gap and DOI, while

Figure 2.11: The range of *charge sharing effect* changes with different gaps and depths of interactions (DOI) with the bias voltage $V = 300$ V. The range of charge sharing decreases as DOI increases as well as the gap size increases. It is ~ 99 μm with gap size $g = 50$ μm at DOI = 0.4 mm.

the bias voltage is kept at 300 V. For the same gap, the range of *charge sharing effect* decreases when DOI increases. In other words, a small DOI brings a larger range of *charge sharing effect*. It is because the electron cloud would expand much wider if it had more traveling time or distance within the detector to couple to the adjacent anode leading to a simpler way to induce charges on adjacent anodes (Equation 2.4).

For instance, the range of *charge sharing effect* decreases from ~ 111.5 μm while DOI = 0.4 mm to ~ 31.5 μm while DOI ≈ 4 mm with gap $g = 25$ μm. Moreover, the range of *charge sharing effect* has an approximately linear relationship with DOI, especially with smaller DOI, which is because the weighting potential is linear to DOI near the cathode. On the other hand, when the gap is narrower, the range of *charge sharing effect* is more significant. For example, the range of *charge sharing effect* decreases from ~ 111.5 μm while $g = 25$ μm to ~ 61.5 μm while $g = 125$ μm at DOI = 0.4 mm. Especially, for

some large gaps, there would be no *charge sharing effect* at all if the DOI were beyond a certain value. For example, at DOI = 3.6 mm while $g = 125$ μm or DOI = 4.0 mm while $g = 100$ μm. A gap of $g = 50$ μm, where the range of *charge sharing effect* is ~ 99 μm when DOI = 0.4 mm and ~ 19 μm when DOI ≈ 4 mm, was selected to be the gap value in later simulations. Because large gap causes significant energy loss on anodes, the gap size should be as small as possible. Another important reason for this selection is that the range of most of the photoelectrons is less than 40 μm with 120 keV X-ray radiation, (as describeded in Section 2.2.3), and a gap $g = 50$ μm could efficiently prevent most cross talk effect.

Figure 2.12 shows the range of *charge sharing effect* changing with bias voltage and DOI, while gap $g = 50$ μm. For the same gap and DOI, the range of *charge sharing effect* decreases when bias voltage increases. In other words, a small bias voltage brings a larger range of *charge sharing effect*, because the spread of the electron cloud would be restricted by the stronger bias voltage. It is also understood that an electron has less traveling time within a detector due to the stronger internal electrical field.

In this figure, the range of *charge sharing effect* decreases from ~ 171 μm while $V = 100$ V to ~ 53 μm while $V = 900$ V at DOI = 0.4 mm, and from ~ 49 μm while $V = 100$ V to ~ 2 μm while $V = 900$ V at DOI ≈ 4 mm. The influence of the change of bias voltage on the range of *charge sharing effect* becomes less and less as the bias voltage increases, which is represented as curves get closer. Since larger bias voltage brings bigger leakage current between anode and cathode, and the charged particles have longer transit time with a small bias voltage, which makes the electrodes could not collect all the charged particles within the collecting time. A voltage $V = 300$ V was selected to be the bias voltage value in later simulations, with which the range of *charge sharing effect* drops from 99 μm at DOI = 0.4 mm to ~ 19 μm at DOI ≈ 4 mm.
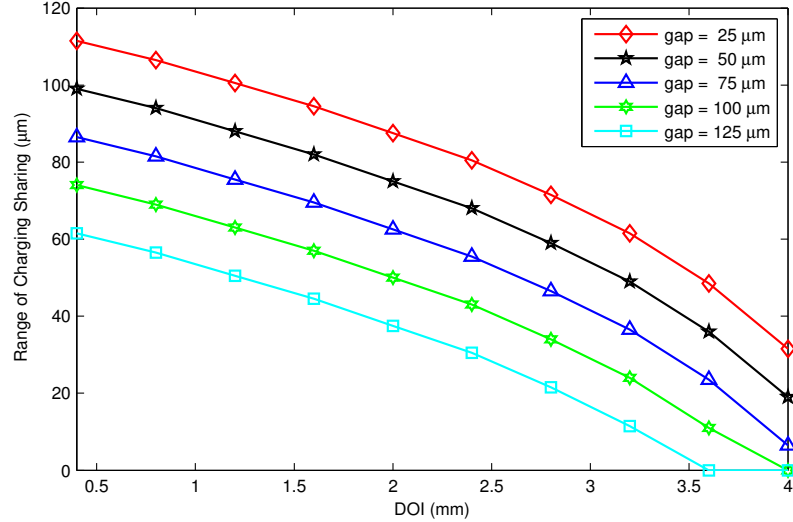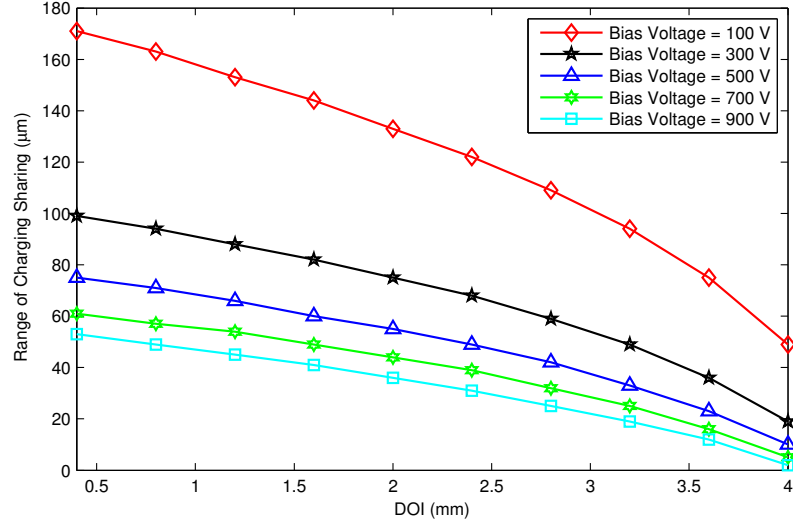
Figure 2.12: The range of *charge sharing effect* changes with different bias voltages and depth of interactions (DOI) with the gap $g = 50$ μm. The range of charge sharing decreases as DOI increases as well as the bias voltage increases. It is ~ 99 μm with the bias voltage $V = 300$ V at DOI $= 0.4$ mm.

2.3.3 Intensity of Collecting Signal

To evaluate the signal intensity with *charge sharing effect*, which is called the collecting signal, between two adjacent anodes, an X-ray point source, which keeps emitting 60 keV and 120 keV X-ray photons vertically to the anode plane, moves from the central line of an anode to the adjacent right anode's parallel with the anode plane and at stops for same time every 10 μm along its path. In this simulation, the central line of the gap is set to be $x = 0$.

Figure 2.13 shows the signal intensity on two adjacent anodes, left-side anode and right-side anode, I_{AL} and I_{AR}, with anode size $a = 200$ μm, gap size $g = 50$ μm and bias voltage $V = 300$ V. The noise is not considered here, so the *SNR* is infinite.

With this configuration, the signal intensity on the left-side anode, I_{AL} drops from 1 to 0 gradually, while I_{AR} grows from 0 to 1 on the right-side anode. It could be understood
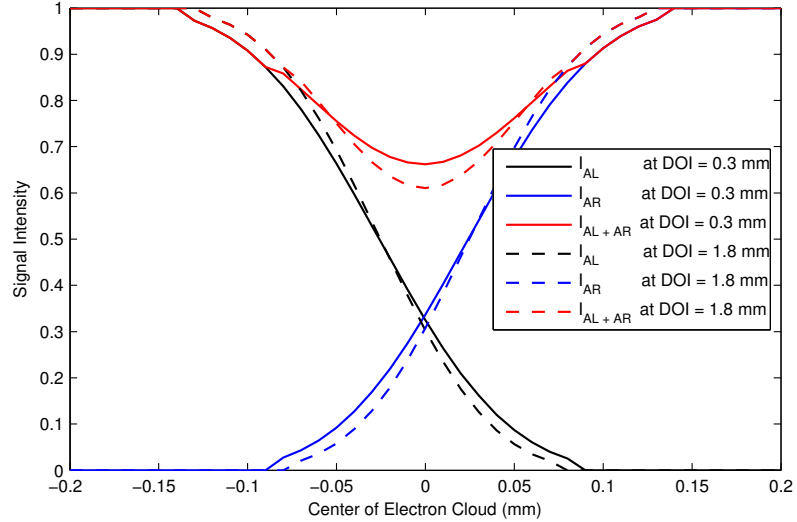
Figure 2.13: Collecting signal intensity due to *charge sharing effect* on adjacent anodes. With a smaller depth of interaction, the range of charge sharing is wider and the energy loss is less. $x = 0$ represents the central line of the gap, where the total energy collected lost most.

as the anode is unable to collect electrons to generate a signal if the center of electron cloud were too far away to couple the anodes. Besides, for DOI $= 0.3$ mm, *charge sharing effect* occurs on the adjacent anode when the absolute position of the X-ray point source is $|x| = 90~\mu m$, while it is $|x| = 80~\mu m$ when DOI $= 1.8$ mm. The red lines represent the sum signal Intensity of two anodes, however, it is less than 1 if the interaction occurs close to the edge of the anode or within the gap due to the dominance of *charge sharing effect*, which means energy lost in the area. Specifically, it is 0.6621 and 0.6104 while DOI $= 0.3$ mm and DOI $= 1.8$ mm when the center of the electron cloud is on the central line of the gap, $x = 0$, respectively. The size of the area that energy is lost is twice the gap size approximated from Equation 2.8. Futhermore, this area is negatively related with DOI.

50

2.4 Transit Signal

2.4.1 *Shockley-Ramo Theorem*

In order to evaluate the transit signal on the electrode, Shockley (Shockley, 1938) and Ramo (Ramo, 1939) developed the *Shockley-Ramo Theorem* independently, which states the expression of induced charge Q as:

$$Q = -q\varphi_0(\underline{x}) \tag{2.9}$$

$$i = q\vec{v} \cdot \vec{E}_0(\underline{x}) \tag{2.10}$$

where $\vec{v}$ is the instantaneous velocity of moving charge q, $\varphi_0(\underline{x})$ is the electric potential or weighting potential, and $\vec{E}_0(\underline{x})$ is the build-in electric field or weighting field at $\underline{x} = (x, y, z)^T$, the position for consideration when the target anode at unit potential and cathode at zero potential (while no other anode is charged and their are no other charges within the area).

The *Shockley-Ramo Theorem* could be used to estimate the transit signal on electrodes of an apparatus with stationary space charge as Equation 2.9, such as a semiconductor detector with a constant voltage difference applied between anode and cathode (Shockley, 1938) since it assumes to ignore the magnetic influence and consider electric field instantaneously. The induced charge Q on the electrode is always less than the original charge q due to the weighting potential $\varphi_0(\underline{x}) < 1$.

2.4.2 Weighting Potential

To obtain the distribution of weighting potential with a particular CZT detector configuration, using the *Shockley-Ramo Theorem* a series of models were built with $L = 4.0\ mm$ and $a = 0.4\ mm \sim 4.0\ mm$ and a single anode with unit voltage and cathode with no voltage.
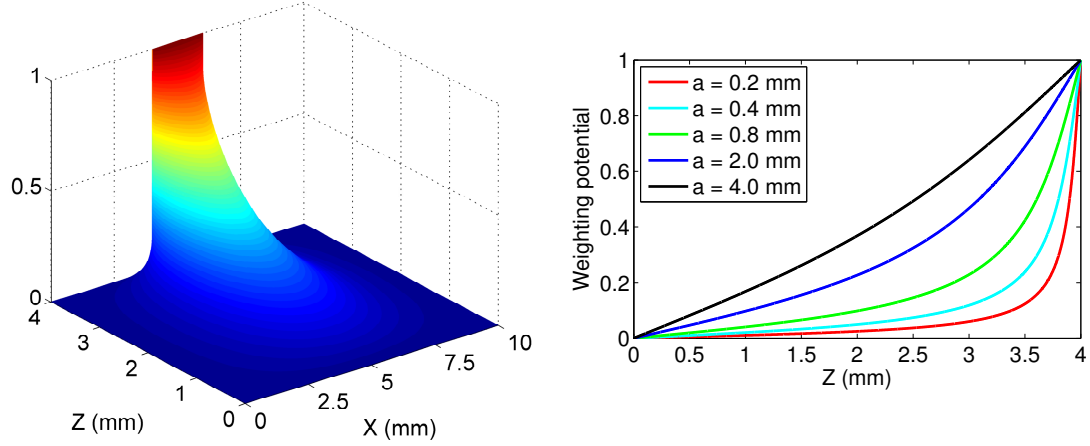
Figure 2.14: Weighting potential within a CZT detector. Left: the weighting potential distribution of anode size $a = 2.0\ mm$ and detector thickness $L = 4.0\ mm$. Right: The weighting potential profiles of different anode size range $0.2 \sim 4.0\ mm$ along the central line of the anode.

In Figure 2.14, the left figure shows the weighting potential distribution of anode size of $a = 2.0\ mm$ and detector thickness of $L = 4.0\ mm$, while the right figure shows the different weighting potential profiles with different anode sizes from $0.2\ mm$ to $4.0\ mm$ along the central line of the anode. Since X-rays hit the cathode first and then run inside the CZT crystal, $z = 0.0\ mm$ and $z = 4.0\ mm$ represents cathode and anode surface of CZT detector respectively. Actually, the weighting potential does not increase linearly from the cathode plane to the anode plane. As reducing the proportion between the size of the anode to the thickness of the detector, the weighting potential within the area near the cathode increases more slowly but more aggressively near the anode, which is called the *small pixel effect* (He, 2001) (right plot of Figure 2.14). With the small pixel effect, the same distance close to anode that electrons move toward would induce more charge, if the anode were to be smaller, and the detector would be more sensitive to spatial location of interactions. However, other effects would also be involved, such as *charge sharing effect* (Veale *et al.*, 2011).

2.4.3   Transit Signal on Anode

With the *Shockley-Ramo theorem* Equation 2.9, it is easy to calculate the charge on a specific electrode as induced by charged particles released from a single incident photon at the specific position inside the CZT detector. Especially, when the charged particles move from position $\underline{x_0}$ to position $\underline{x_t}$ within time t, the induced charge Q_t on the electrode could be described as:

$$Q_t = -qN_e[\varphi(\underline{x_t}) - \varphi(\underline{x_0})] \tag{2.11}$$

where N_e is the total number of electrons created by the incident photon. q could be positive or negative in charge dependending on the type of charge carrier. The negativesign indicates the polarity of the transit signal is opposite from the original charged particle. This indicates the transit signal on the electrode is related to the starting and ending position as well as the weighting potential within the CZT detector. This in turn is related to the size of the electrode, or more precisely, the ratio between the thickness of the detector and the size of the electrode.

Moreover, given the weighting potential of the cathode and anode are 0 and 1 respectively, the total induced charge on both anode and cathode when all charge carriers, electrons and holes reach electrodes without considering trapping or collecting time limit is represented as

$$
\begin{aligned}
Q' &= qN_{eh}[1 - \varphi(z_0)] + (-qN_{eh})[0 - \varphi(z_0)] = qN_{eh} & (2.12) \\
N_{eh} &= N_e = N_h & (2.13)
\end{aligned}
$$

In order to clearly state the position of interaction inside the CZT detector, two parameters are used in this thesis: lateral offset (LO) and depth of interaction (DOI). As shown in Figure 2.15, LO is the distance between the point of interaction and the central line of
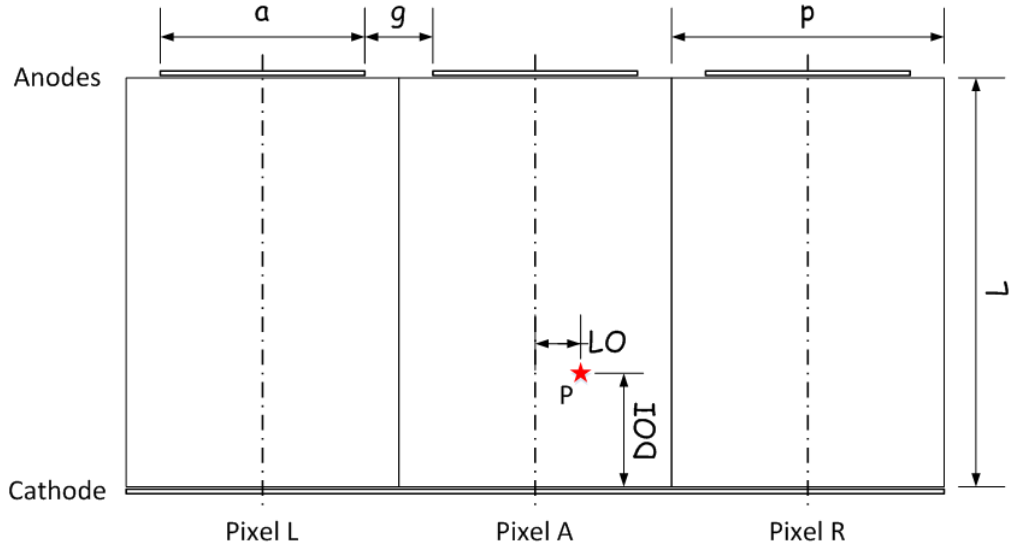
Figure 2.15: Definition of the interaction position inside the CZT detector. The position is defined with lateral offset (LO) and depth of interaction (DOI). LO is the distance between the point of interaction and the central line of pixel-of-interesting (Pixel A). DOI is the depth between the point of interaction and the cathode plane.

pixel-of-interest (Pixel A). LO is positive if it is at the right side of the central line and closer to the *Anode R* but negative if the other way around. DOI is the depth between the point of interaction and the cathode plane, as defined in Section 1.4.2.

Figure 2.16 illustrates the normalized transit signal on the anode generated by moving a unit negative charge with different DOIs inside the CZT detector and different ratios of thickness of detector and size of the anode. As described in Section 2.2.4, the velocity of the electron $v_e \approx 7.5 \times 10^3$ m/s when the bias voltage $V = 300$ V. Because of the high mobility of electrons within CZT crystal, they are assumed to be collected by the anode in time, for instance, all electrons would be collected in approximately 500 ns even if they were released 3.7 mm away from the anode. The final transit signal increases as DOI decreases with the same ratio of thickness of detector and size of anode, because with a smaller DOI, the position that is closer to the cathode, a certain number of electrons have more electric
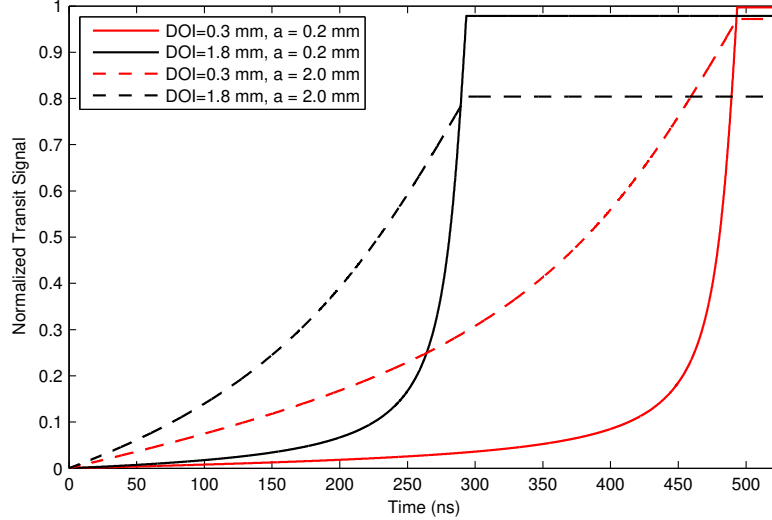
Figure 2.16: Normalized transit signal on a single anode with different anode sizes and depth of interactions (DOIs). The initial charge was released on the central line of the pixel with a bias voltage of 300 V. For the same DOI (same colour), the final transit signal is larger with a smaller pixel (solid line) than a bigger pixel (dash line).

potential. Because of small pixel effect, with the same DOI, a certain amount of electrons have more electric potential with a smaller pixel than a bigger one. Therefore, for the same DOI, the final transit signal is larger with smaller pixels (solid line).

Figure 2.17 shows the normalized transit signal on two adjacent anodes, with detector thickness $L = 4.0$ mm, size of anode $a = 0.4$ mm, gap between two adjacent anodes $g = 100$ μm and bias voltage $V = 300$ V, while the interaction took place at DOI $= 0.3$ mm and DOI $= 1.8$ mm on the central line of *anode A*. For the *anode A*, the final transit signal was always less than 1, which means no energy lost. The small deficiency of energy is because of DOI > 0.

Generally, the transit signal on *anode R* increased slowly when electrons were far enough from anodes, but decreased quickly when they came into the area that *anode A* dominates, where the weighting potential line from *anode A* is tangential to the electrons' trajectory.
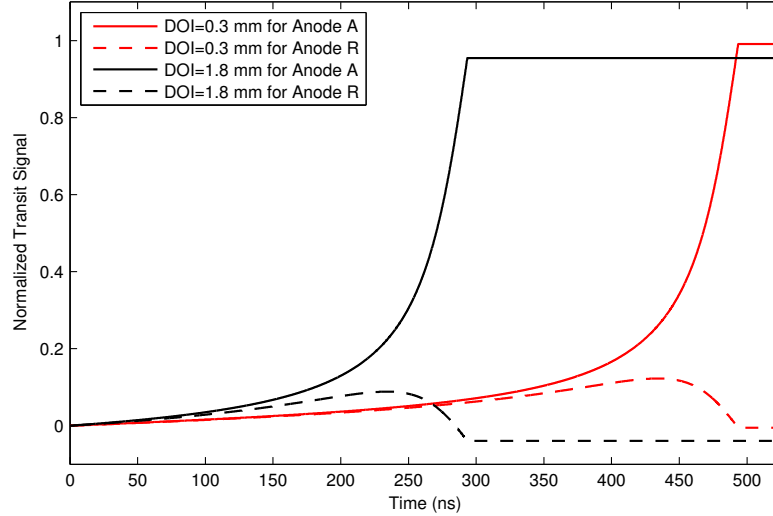
Figure 2.17: Normalized transit signal on collecting anode and neighbouring anode. Here the thickness of detector $L = 4.0\ mm$, the size of anode $a = 0.4\ mm$, the gap between the two anodes $g = 100\ \mu m$ and bias voltage $V = 300\ V$, and positions of interactions were DOI $= 0.3$ mm and DOI $= 1.8$ mm on the central line of collecting anode respectively.

In this procedure, the value of the transit signal on *anode R* could be affected by the ratio of the thickness of the detector to the anode size L/a, the size of gap g and the starting point of electrons inside detector $\underline{x_0}$.

Figure 2.18 shows the normalized transit signal on the adjacent *anode R* with different interaction positions, while the thickness of detector $L = 4.0\ mm$, with the anode size $a = 0.4\ mm$, the gap size $g = 100\ \mu m$ and the bias voltage $V = 300\ V$. LO $= 0.00$ mm means the interaction took place on the central line of *anode A* and LO $= 0.25$ mm in the middle of two adjacent anodes since the pitch $p = a + g = 500\ \mu m$. It could be observed that with the same DOI, the maximum value of transit signal increased as LO increased, indicating more charges were induced on the neighboring anode with a closer electron cloud. It has to be mentioned that with the same LO the difference between maximum and minimum values of transit signal did not change as DOI (which are $0.1283Q$,
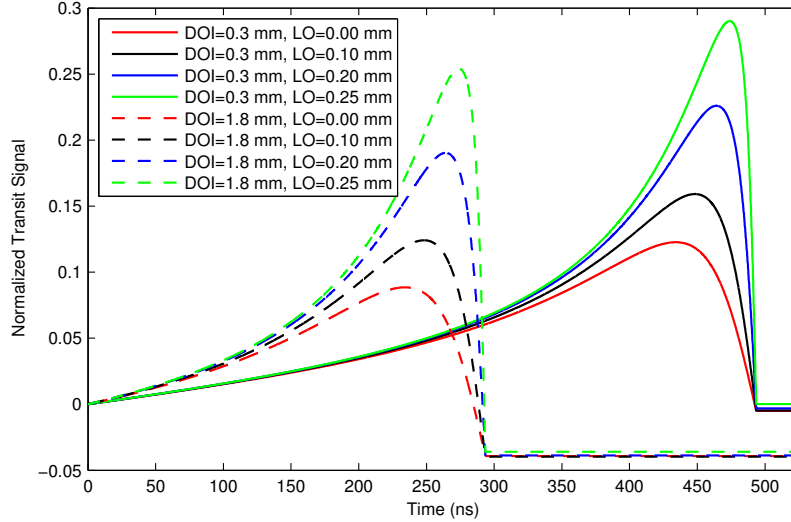
Figure 2.18: Normalized transit signal effect on neighbouring anode with different lateral offests (LOs) and depths of interactions (DOIs). Here the following were used: thickness of detector $L = 4.0$ mm, the size of anode $a = 0.4$ mm, the gap between the two adjacent anodes $g = 100$ μm and bias voltage $V = 300$ V. The solid lines represent interactions with DOI = 0.3 mm and the dashed lines represent interactions with DOI = 1.8 mm.

$0.1649Q$, $0.2318Q$ and $0.2959Q$ for LO = 0.00 mm, LO = 0.10 mm, LO = 0.20 mm and LO = 0.25 mm respectively). Moreover, a bigger DOI ends up with a lower minimum value, indictating negative charge carriers have more electric potential when they are further away from the anode.

2.4.4   Intensity of Transit Signal

Here three contiguous pixels are evaluated, where the middle one is assumed as the collecting anode while the side two are minor-collecting anodes. To evaluate the signal intensity with charge inducing effect (referred to as transit signal), on the two minor-collecting anodes, an X-ray point source, which keeps emitting 60 keV and 120 keV X-ray photons vertically

to the anode plane, moves from the central line of the gap between the left-side minor-collecting anode and collecting anode to the central line of the gap between the right-side minor-collecting anode and collecting anode parallel with the anode plane, sopping briefly every 10 μm along the path. In this simulation, the central line of the collecting anode was set to be $x = 0$.

Figure 2.19 shows the maximum signal intensities on two minor-collecting anodes, left-side and right-side, I_{NL} and I_{NR} with the different lateral position of interactions, with anode size $a = 0.4\ mm$, gap size $g = 100\ \mu m$. While the electrons move toward the anode plane, charges are induced both on the collecting and neighbouring anodes and are known as the transit signal (Figure 2.17). The signal intensity depends on the lateral position of the *photoelectric effect* taking place, the anode size and the gap size. To be exact, the signal intensity would be larger if the position of the *photoelectric effect* taking place were closer to the anode.
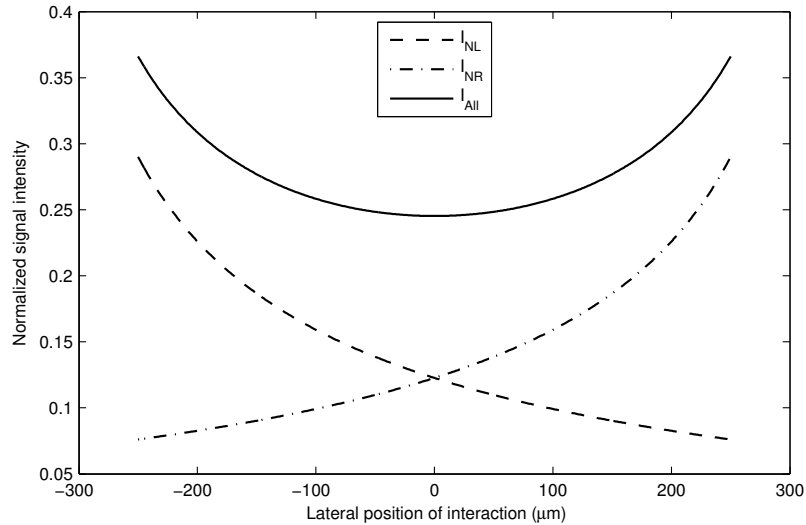
Figure 2.19: Transit signal intensity on neighbouring minor-collecting anodes. $x = 0$ represents the central line of the collecting anode, where the total energy lost was maximal.

The noise was not considered here, so the SNR was infinite. With this configuration, the transit signal intensity on the minor-collecting anodes changed from $0.0761Q$ to $0.2901Q$ monotonically, and the minimum value of total signal intensities both on the two minor-collecting anodes was $0.2453Q$ at $x = 0$.

Chapter 3

Sub-Pitch Spatial Resolution

Achievement

As previously described, when the X-ray photon deposits its energy inside the CZT detector, the coordinate of its electron cloud center $\underline{x} = (x, y, z)^T$ represents the position of interaction. This means the position of interaction could be achieved with an investigation on the distribution of the electron cloud. The accuracy of this coordinate estimation would allow determination of spatial resolution.

Generally, the spatial resolution is up to the pixel size on the detector. In the best situation, the FWHM of the LSF equals three times the pixel size (Equation 1.12). For example, a detector with pixel size $p = 0.5\ mm$ could not provide the FWHM of LSF better than $0.5 \times 3 = 1.5\ mm$, which is too large for the proposed clinical applications. On the other hand, reducing the pixel size seems to be a straightforward method to increase spatial resolution, but this would bring many problems at the same time, such as 1) unacceptable cost to fabricate circuitry for small pixels and 2) limitation of improvement of spatial resolution from charge sharing effect and cross talking effects.

3.1   Intensity Comparison Method

To achieve spatial resolution with precision better than the pitch size, a simple and straight method is the intensity comparison method. This determines coordinates of the interaction when comparisons are made in intensities from different groups of anodes.

In Figure 3.1, the red dot represents an interaction. Its collecting pitch $P(0,0)$ is divided into four quadrants equally as shown. The circle represents the area that would yield signal on the anodes.
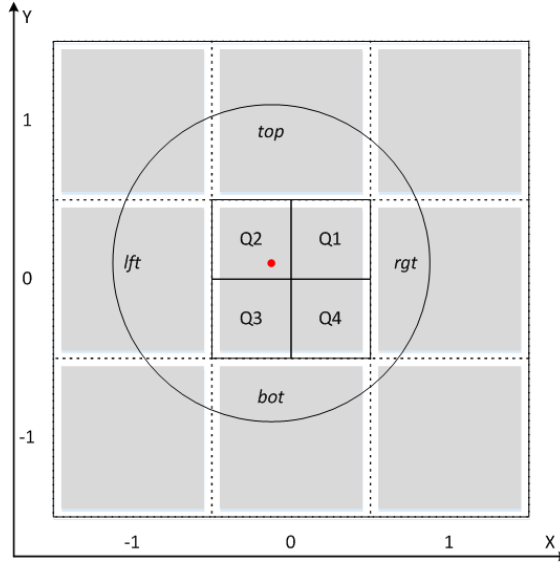
Figure 3.1: Schematic representation of the comparison method: to locate the quadrant that the interaction takes place, compare the signal intensities on different groups of anodes, and the closer interaction brings larger signal intensity.

$$I_{top} = I_{P(-1,1)} + I_{P(0,1)} + I_{P(1,1)} \tag{3.1}$$

$$I_{bot} = I_{P(-1,-1)} + I_{P(0,-1)} + I_{P(1,-1)} \tag{3.2}$$

$$I_{lft} = I_{P(-1,-1)} + I_{P(-1,0)} + I_{P(-1,1)} \tag{3.3}$$

$$I_{rgt} = I_{P(1,-1)} + I_{P(1,0)} + I_{P(1,1)} \tag{3.4}$$

In order to locate the quadrant with the source of interaction, a comparison between signal intensities on the different groups of anodes is necessary and adequate. It is common sense that the closer an interaction the larger the signal intensity. In detail, one would calculate four sums of signal intensities on top-side, bottom-side, left-side and right-side of the collecting pitch respectively as Equation 3.1-Equation 3.4 shown, and then the quadrant of the interaction is determined easily using Table 3.1.

Table 3.1: Determination for quadrant of interaction

Quadrant	$I_{lft} > I_{rgt}$	$I_{lft} < I_{rgt}$
$I_{top} > I_{bot}$	Q2	Q1
$I_{top} < I_{bot}$	Q3	Q4

Although determination of the interaction quadrant might be uncertain, due to signal intensity error caused by electronic noise or some other hardware factor, if the interaction takes place close enough to the boundary of quadrants it is able to achieve sub-pitch spatial resolution at about half pitch size for most of the events.

For example, for a configuration of detectors with anode size of $a = 0.2\ mm$ and gap size of $g = 50\ \mu m$, meaning pitch size is $p = a + g = 250\ \mu m$, the sub-pitch spatial resolution is achieved as $SR_{ICM} \sim p/2 = 125\ \mu m$ with *intensity comparison method*. Even though this is simple it is still not good enough for clinical application. Thus other methods need investigation.

3.2 Intensity Difference Method

In *intensity comparison method*, comparable intensities on different anode groups were just used to achieve the rough range of the interaction taking place. It is only a qualitative analysis and the result is not good enough.

Considering the quantitative analysis, a certain relationship between the distance from

the interaction to the anode and the signal intensity is required. The difference between two comparable signal intensities is able to provide more detailed spatial information, named as the *intensity difference method*, which is defined as (Allwork *et al.*, 2012; Zheng *et al.*, 2016):

$$f_d \quad = \quad I_1 - I_2 \tag{3.5}$$

where I_1 and I_2 are the two comparable signal intensities on different anodes. Both transit signal and collecting signal are considered for use with this method.

3.2.1 Using Transit Signal

Transit signal has a pretty wide range to yield signals on anodes due to the *charge inducing effect*. The value of the transit signal intensity depends on the lateral position of the interaction. In other words, the transit signal intensity would be larger if the interaction were closer to the anode and vice versa. This is a specific relationship between the position of the interaction and the signal intensity.

According to Equation 3.5, the difference between transit signal intensities on two minor-collecting anodes, neighbouring the collecting anode, is:

$$f_{DTS} \quad = \quad I_{TNR} - I_{TNL} \tag{3.6}$$

where I_{TNR} and I_{TNL} are transit signal intensity on right-side neighbouring minor-collecting anode and left-side neighbouring minor-collecting anode respectively.

Based on the simulation model in Figure 2.19, with bias voltage of $V = 300\ V$ and detector thickness of $L = 4\ mm$, the anode size increases from $a = 0.2\ mm$, $a = 0.4\ mm$, $a = 0.8\ mm$ to $a = 2.0\ mm$ and gap size is kept to be $g = a/4$. The central line of the

Figure 3.2: Profile of transit signal intensity differences with different anode and gap sizes of $g = a/4$. 1. Anode size $a = 0.2\ mm$; 2. Anode size $a = 0.4\ mm$; 3. Anode size $a = 0.8\ mm$; 4. Anode size $a = 2.0\ mm$.

collecting anode was set as $x = 0$. An X-ray point source, which keeps emitting 60 keV and 120 keV X-ray photons vertically to the anode plane, moves from the central line of the gap between the left-side minor-collecting anode and collecting anode to the central line of the gap between the right-side minor-collecting anode and collecting anode parallel with the anode plane. It stops for the same length of time every 10 μm along its path, and at each stop, 1000 interactions were taken for assessment.

The maximum of f_{DTS} increased from 0.2133, 0.2140, 0.2198 to 0.2306 in four models respectively, shown in Figure 3.2. The blue dash lines represent the area of the collecting anode. There was an approximately linear relationship between f_{DTS} and x around the area of the collecting anode, as indicated by the red dash-dot line, which can be interpreted as f_{DTS} being used to achieve spatial resolution.
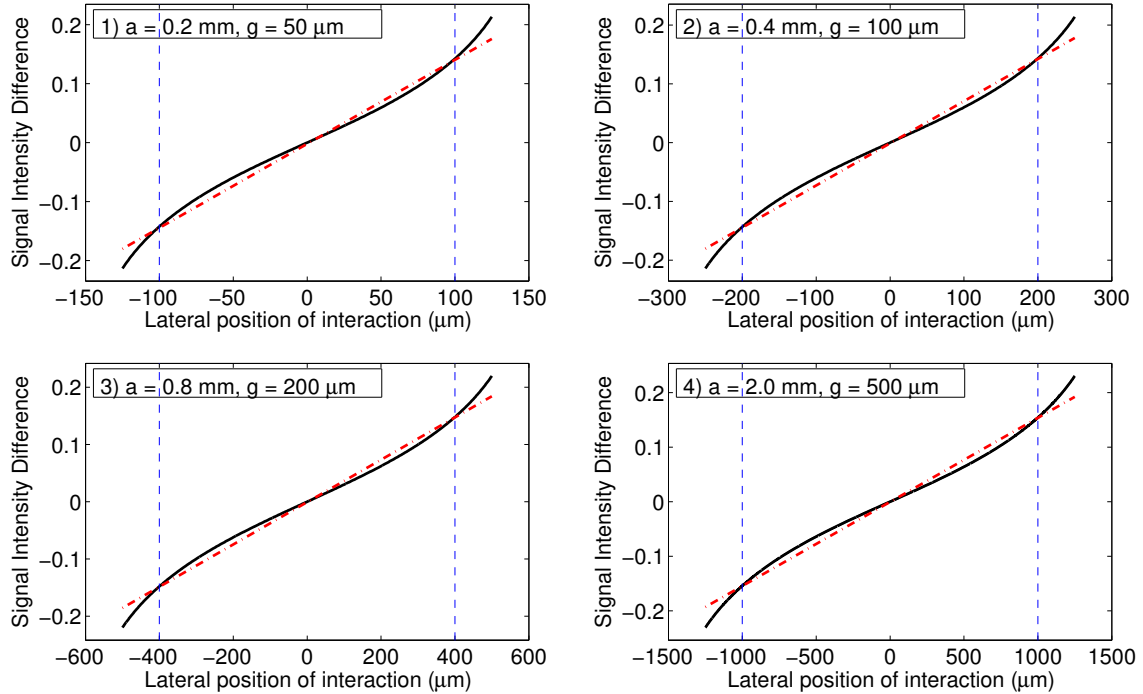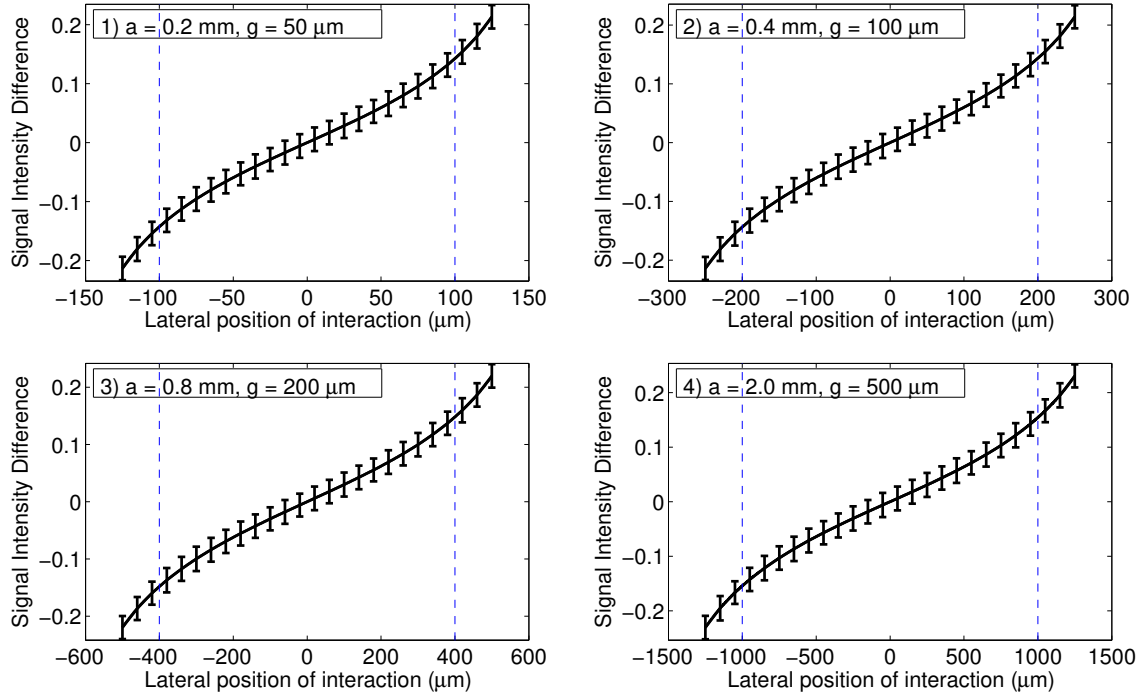
Figure 3.3: Errorbar of transit signal intensity differences with different anodes and gap size of $g = a/4$. 1. Anode size $a = 0.2\ mm$; 2. Anode size $a = 0.4\ mm$; 3. Anode size $a = 0.8\ mm$; 4. Anode size $a = 2.0\ mm$.

Unlike the anode size, the gap size is not that important to f_{DTS}, since the weighting potential matrix is generated by a single anode all the time and there is always only one collecting anode for one interaction. Besides, the gap size was always much less than anode size.

However, the linear relationship deteriorates when x is far enough away from the central line of the collecting anode. This was because one of the two transit signal intensities became weaker and weaker, when x moved too far away from the anode to yield transit signal. In this situation, f_{DTS} appears to more likely depend on single transit signal intensity.

On the other hand, in order to estimate the value of sub-pitch spatial resolution, noise in the CZT detector must be considered. The previous study showed that anticipated noise could be modeled as a Gaussian (Makeev *et al.*, 2013). In this thesis, the detector SNR was

defined as the ratio of the amplitude of the X-ray photopeak to the standard deviation of the noise floor. This was set as 15 for all simulations.

Figure 3.3 shows error bars for the transit signal intensity differences with different anode and gap size of $g = a/4$. It should be noted that the interval between points (samples) was every 10 μm, 20 μm, 40 μm and 100 μm respectively for the purpose of clearly showing the effect of distance (resolution).

Thus, the sub-pitch spatial resolution was achieved as the minimum lateral distances without overlapping error bars, as shown in Table 3.2. It is about one-sixth of the pitch size approximately.

Table 3.2: Spatial resolution with transit signal intensity differences.

Anode(mm)	0.2	0.4	0.8	2.0
Gap(μm)	50	100	200	500
SP(μm)	$\in (30, 40)$	$\in (60, 80)$	$\in (120, 160)$	$\in (300, 400)$

The spatial resolution of the *intensity difference method* with transit signal is sub-pitch, but the profile of f_{DTS} is not very linear to the lateral position x. Thus the spatial resolution still has room for improvement.

3.2.2   Using Collecting Signal

Due to charge sharing effect, the two adjacent anodes collect part of the electron cloud and yield collecting signal respectively. The value of the collecting signal intensity depends on the lateral position of the center of the electron cloud. In detail, around the area of the gap between two anodes, the signal intensity would be larger if the center of electron cloud were closer to the anode and vice versa. The signal intensity on each adjacent anode shows a linear relationship with the lateral position of the center of the electron cloud, which is also the position the interaction between radiation and CZT material taking place. It

means the position of the center of the electron cloud could be represented with collecting signal intensities on two adjacent anodes. According to Equation 3.5, the difference between collecting signal intensities on two adjacent anodes is represented as:

$$f_{DCS} \quad = \quad I_{CAR} - I_{CAL} \tag{3.7}$$

where I_{CAR} and I_{CAL} are collecting signal intensity on the right-side adjacent anode and left-side adjacent anode respectively.

Based on the simulation model in Figure 2.13, an X-ray point source, which keeps emitting 60 keV and 120 keV X-ray photons vertically to the anode plane, moves from $x = -200\ \mu m$ to $x = 200\ \mu m$ paralleling with the anode plane. It stops for the same length if time every 10 μm along its path, and at each stop, 1000 interactions were taken for the investigation. With DOI $= 0.3$ mm, bias voltage of $V = 300\ V$ and detector thickness of $L = 4\ mm$, the gap size increases from $g = 25\ \mu m$ to $g = 100\ \mu m$ with 25 μm increment each time. f_{DCS} increases from -1 to 1 monotonically as lateral position x moves towards the right, shown in Figure 3.4. The blue dash lines represent the area of the gap and central line of the gap between the two adjacent anodes is set to be $x = 0$. There is a good linear relationship between f_{DCS} and lateral position x around the area of the gap, as shown with the red dash-dot line, thus proving f_{DCS} could be used to achieve spatial resolution.

However, the linear relationship deteriorates when x is far enough away from the gap area. It is because one of two collecting signal intensities becomes progressively weaker, even becomes 0, when x moves too far away from the anode to yield any collecting signal. In this situation, f_{DCS} depends on single collecting signal intensity absolutely. This could also explain why the slope of the curve becomes smaller as the gap becomes wider. Due to loss of charge within the gap, the electron cloud is increasingly more unlikely to be fully collected by two adjacent anodes concurrently as the gap grows. On the other hand, unlike
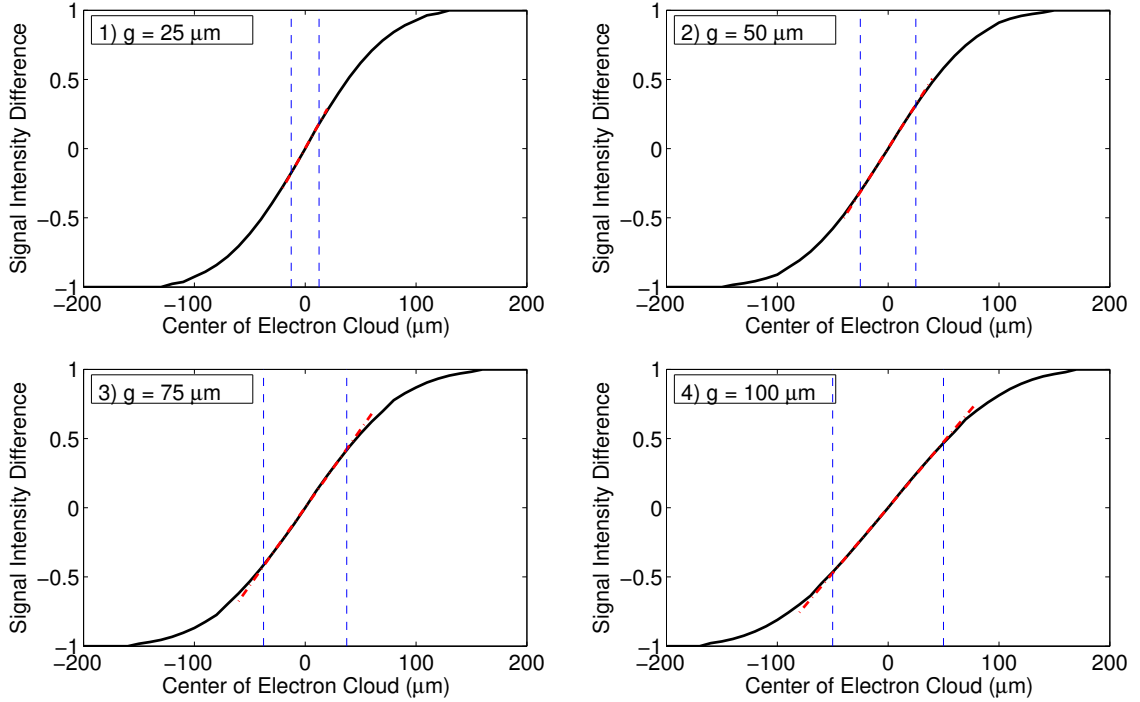
Figure 3.4: Profile of collecting signal intensity differences with different gaps. 1. Gap size $g = 25$ μm; 2. Gap size $g = 50$ μm; 3. Gap size $g = 75$ μm; 4. Gap size $g = 100$ μm.

gap size, anode size is not that important to f_{DCS}, since anode size is always kept much bigger than the range of the *charge sharing effect*, which is approximate 111.5 μm while DOI = 0.4 mm with gap size of $g = 25$ μm (Figure 2.11).

Again, an SNR = 15 is used to estimate the spatial resolution. After analyzing 1000 events at each position of the X-ray point source, Figure 3.5 shows the error associated with collected signal intensity differences. The sub-pitch spatial resolution was achieved as the minimum lateral distances without overlapping error bars (Table 3.3).

Table 3.3: Spatial resolution with collected signal intensity differences.

| Gap(μm)	25	50	75	100
SP(μm)	$\in (10, 20)$	$\in (10, 20)$	$\in (10, 20)$	$\in (20, 30)$
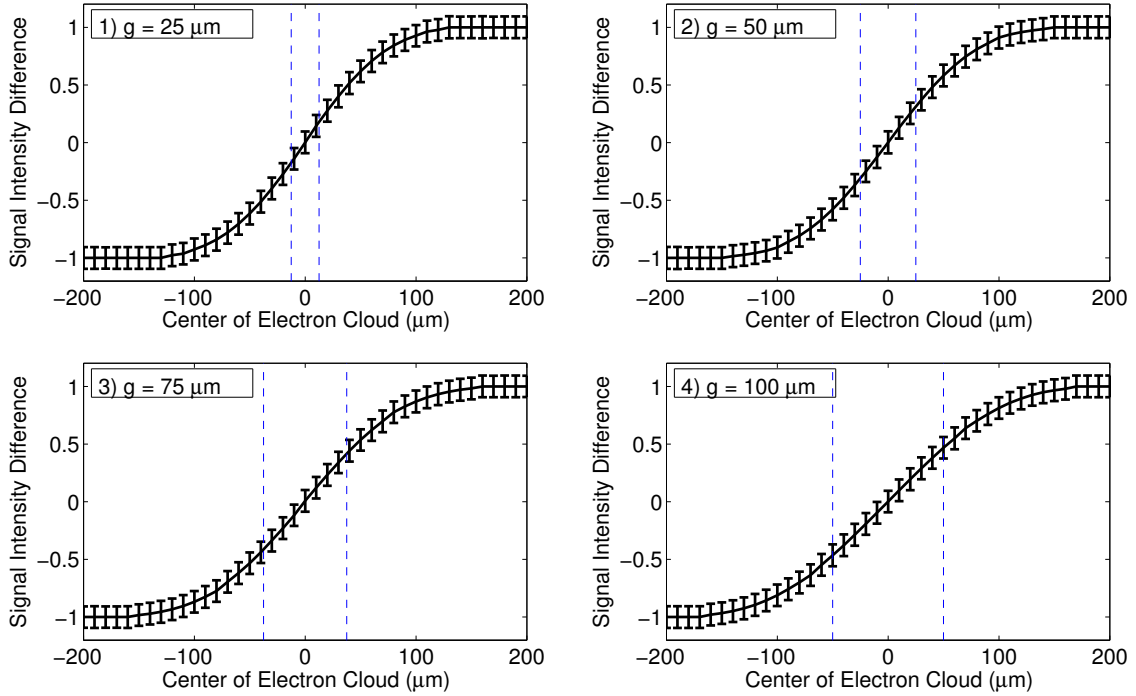
Figure 3.5: Error bar of collected signal intensity differences with differing gaps. 1. Gap size $g = 25~\mu m$; 2. Gap size $g = 50~\mu m$; 3. Gap size $g = 75~\mu m$; 4. Gap size $g = 100~\mu m$.

Compared to the transit signal approach, the sub-pitch spatial resolution method achieved excellent collecting signal, especially around the central line of the gap. But this was based on the *charge sharing effect*.

According to Equation 2.7, it is not hard to estimate the proportion of charge sharing events. $a > g \times 10$ is the condition that distinguishes small gap pixels from big gap pixels. For all configurations between anode size and gap size listed in Table 3.4, more than 30%

Table 3.4: Proportion of charge sharing events.

Anode(mm)	0.2	0.4	0.6	0.4	0.6	0.6
Gap(μm)	25	25	25	50	50	75
$c(\mu m)$	10	12.5	12.5	20	25	30
Proportion	77.81%	46.45%	33.15%	47.52%	32.00%	34.57%

of all events have charge sharing effects included, as well as energy lost, more or less. It should be noted that the proportion of events that could be used to achieve sub-pitch spatial resolution is even lower, since only single *photoelectric effect* events work for obtaining the collecting signal. Besides this point, the spatial resolution achieved deteriorates as the slope of the curve f_{DCS} becomes less when the X-ray point source moves farther from the central line of the gap. This is due to the fact that one of two collected signal intensities is quite small compared to the other. In order to decrease such influences, a better method requires investigation.

3.3   Intensity Ratio Method

An efficient way to get rid of the influence of energy loss is to consider the ratio of the difference to the sum of the intensities, named the *intensity ratio method*. This is defined as (Allwork *et al.*, 2012; Zheng *et al.*, 2016):

$$f_r \;\; = \;\; \frac{I_1 - I_2}{I_1 + I_2} \tag{3.8}$$

where I_1 and I_2 are two comparable signal intensities. Both transit signal and collecting signal are considered for use with this method.

3.3.1   Using Transit Signal

To use the transit signal for the *intensity ratio method*, similar to the *intensity difference method* (Equation 3.8), the ratio of the difference to the sum of the transit signal intensities on two neighbouring minor-collecting anodes is represented as:

$$f_{RTS} \;\; = \;\; \frac{I_{TNR} - I_{TNL}}{I_{TNR} + I_{TNL}} \tag{3.9}$$
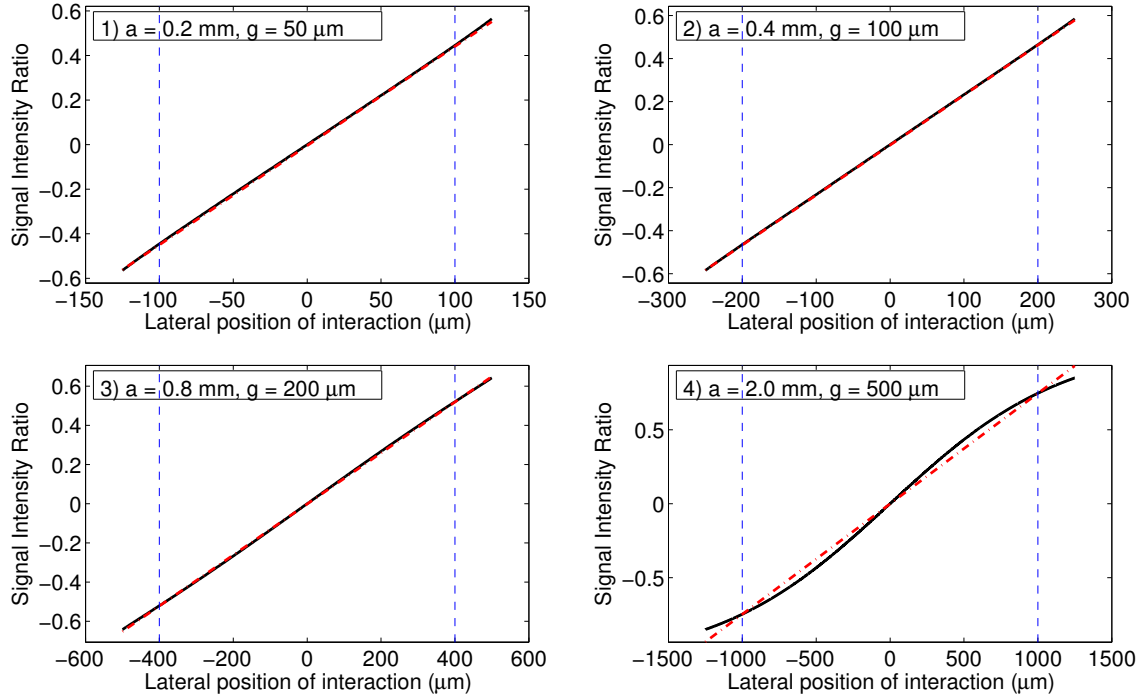
Figure 3.6: Profile of transit signal intensity ratios with different anodes and gap size $g = a/4$. 1. Anode size $a = 0.2\ mm$; 2. Anode size $a = 0.4\ mm$; 3. Anode size $a = 0.8\ mm$; 4. Anode size $a = 2.0\ mm$.

where I_{TNR} and I_{TNL} are the transit signal intensity on right-side and left-side neighbouring minor-collecting anodes, respectively.

Using the simulation in Figure 3.2 again, with bias voltage of $V = 300\ V$, detector thickness of $L = 4\ mm$ and gap size of $g = a/4$, f_{RCS} increases monotonically as the lateral position x moves towards the right (Figure 3.6). It is noted that there is a perfect linear relationship between f_{RTS} and x, as shown by the red dash-dot line. This lies within the region around the collecting anode, as represented by vertical blue dash lines, especially for an anode size of $a \leqslant 0.8\ mm$. This implies that f_{RTS} could be used to achieve better spatial resolution. Moreover, the slope of the profile is steeper than that of the *intensity difference method* after excluding the influence from the energy loss from both adjacent anodes.

Lastly, also with SNR = 15 an estimate of possible spatial resolution is introduced.

71
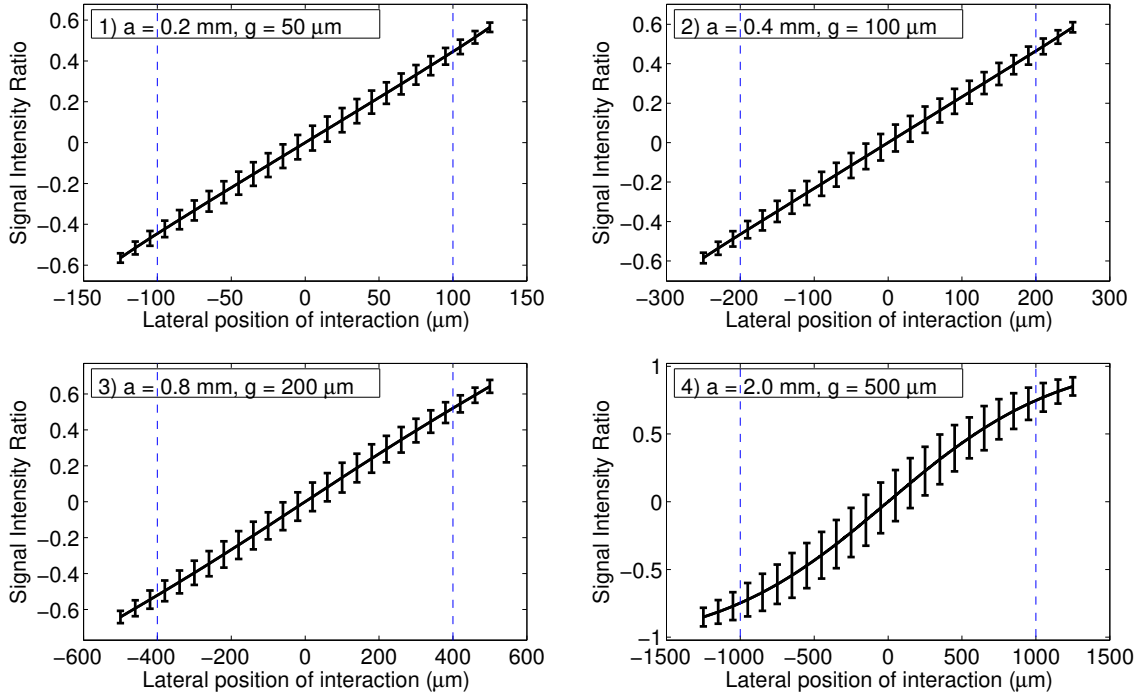
Figure 3.7: Error bar of transit signal intensity ratios with different anodes and gap size $g = a/4$. 1. Anode size $a = 0.2\ mm$; 2. Anode size $a = 0.4\ mm$; 3. Anode size $a = 0.8\ mm$; 4. Anode size $a = 2.0\ mm$.

After analyzing 1000 events at each position of the X-ray point source, Figure 3.7 shows the error in the transit signal intensity ratios with each lateral position. It should be noted that the sampling interval between points was 10 μm, 20 μm, 40 μm, and 100 μm respectively. The sub-pitch spatial resolution was determined as the minimum lateral distances without overlapping errorbars, as shown in Table 3.5, which are about one-eighth of pitch size, or approximately when $a = g \times 4$.

Table 3.5: Spatial resolution with transit signal intensity ratios.

Anode(mm)	0.2	0.4	0.8	2.0
Gap(μm)	50	100	200	500
SP(μm)	$\in (20, 30)$	$\in (40, 60)$	$\in (80, 120)$	$\in (400, 500)$

This approach is thus better than *intensity difference method* with transit signal. For example, when anode size $a = 0.2\ mm$ and gap size $g = 50\ \mu m$, the sub-pitch spatial resolution achieved was between 20 μm and 30 μm. More importantly, the spatial resolution achieved did not deteriorate significantly at either end of the intensity-position curve.

3.3.2   Using Collecting Signal

According to Equation 3.8, the ratio of the difference to the sum of the collecting signal intensities on two adjacent anodes is represented as:

$$f_{RCS} \quad = \quad \frac{I_{CAR} - I_{CAL}}{I_{CAR} + I_{CAL}} \tag{3.10}$$
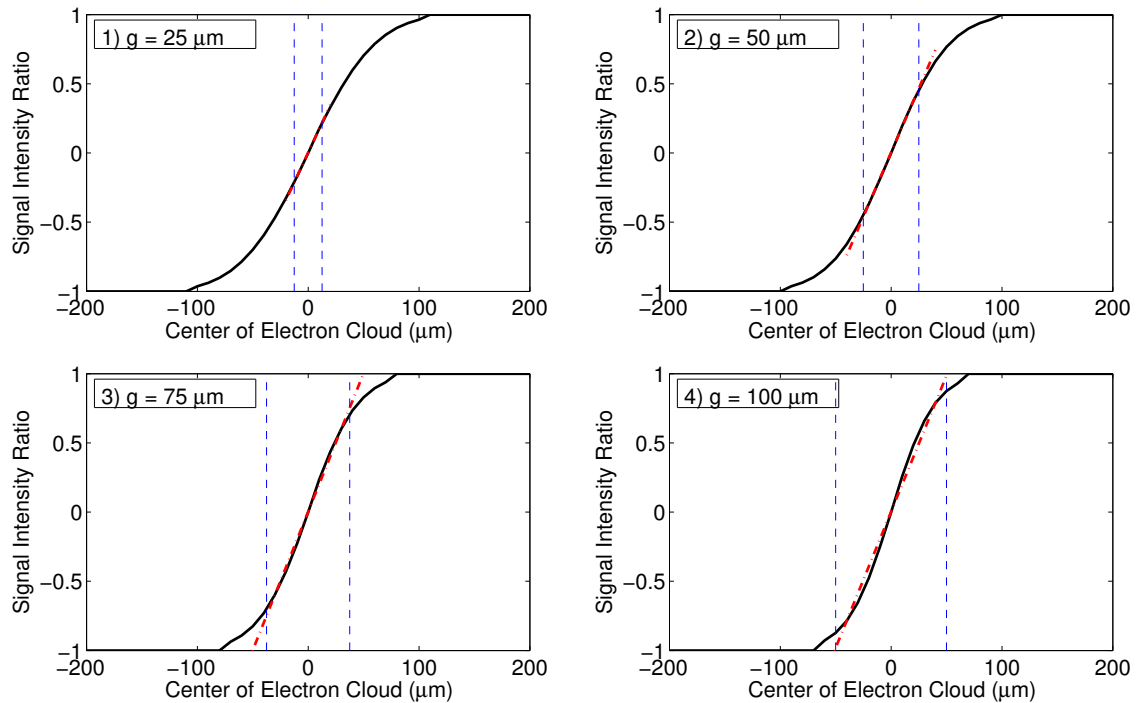
Figure 3.8: Profile of collecting signal intensity ratios with differing gaps. 1. Gap size $g = 25\ \mu m$; 2. Gap size $g = 50\ \mu m$; 3. Gap size $g = 75\ \mu m$; 4. Gap size $g = 100\ \mu m$.

where I_{CAR} and I_{CAL} are collected signal intensities on the right-side adjacent anode and the left-side adjacent anode respectively. Once again, using the simulation detailed in Figure 3.4, with DOI = 0.3 mm, bias voltage of $V = 300$ V and detector thickness of $L = 4$ mm, the f_{RCS} increased from -1 to 1 monotonically as lateral position x moved towards right (Figure 3.8).
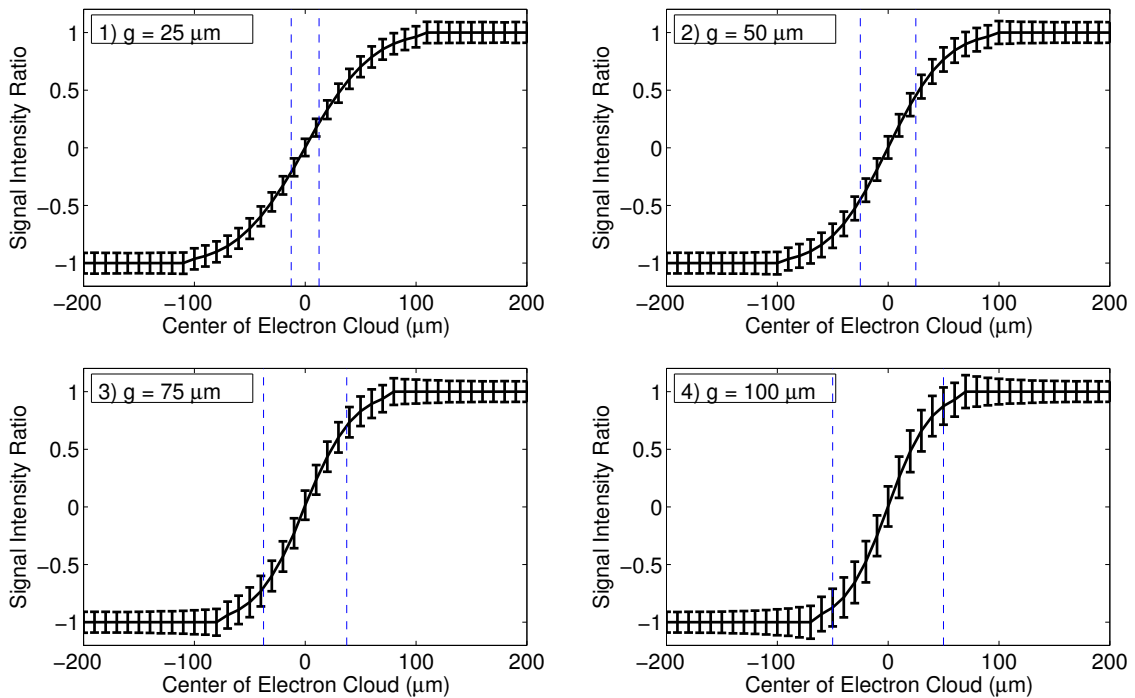
Figure 3.9: Error bars of collecting signal intensity ratios with different gaps. 1. Gap size $g = 25$ μm; 2. Gap size $g = 50$ μm; 3. Gap size $g = 75$ μm; 4. Gap size $g = 100$ μm.

It can be clearly seen that there is approximately a linear relationship, as indicated by the red dash-dot line, between f_{RCS} and x around the area of the gap (represented as blue dash lines). This suggests that f_{RCS} could also be used to achieve spatial resolution. One important point, however, is the slope of the profile is steeper than that of *intensity difference method* after excluding the influence from energy loss. Here, the absolute value

of f_{RCS} reaches 1 faster, where one of the two collecting signals turns to 0. Thus this approach does not provide further improvement in spatial information but rather shows the advantage of the *intensity ratio method* when compared to the *intensity difference method*.

With SNR = 15 an estimate the spatial resolution, after analyzing 1000 interactions at each position for the X-ray point source, is shown in Figure 3.9. This shows the error of collected signal intensity ratios with different lateral positions. The sub-pitch spatial resolution was achieved as the minimum lateral distances without overlapping errorbars (Table 3.6). For example, it was less than 10 μm when gap size of $g = 25$ μm was used, and less than 20 μm when a gap size of $g = 50$ μm around the central line of the gap, was used. This was better than the *intensity difference method* with collecting signal.

Table 3.6: Spatial resolution with collecting signal intensity ratios.

Gap(μm)	25	50	75	100
SP(μm)	$\in (0, 10)$	$\in (10, 20)$	$\in (10, 20)$	$\in (10, 20)$

Chapter 4

Discussion and Conclusions

4.1 Factors Regarding the Detector

In Chapter 2, several factors that affect the pixelated CZT spatial resolution were ana-
lyzed, including X-ray photon energy, depth of interaction (DOI), the lateral offset (LO) of
interaction, the detector thickness, anode size, gap size and bias voltage. The first three
factors depended on the interaction itself, which made the detector output very different
signals. The last four factors belong to the configuration of the detector, which need to
be considered based on the specific clinical application. Since adjusting each factor could
lead to improvement or deterioration of the detector performance, tradeoffs needed to be
evaluated.

4.1.1 X-ray Energy

X-ray photons at the receiving side provides structural information of the patient's body,
after attenuation. It is captured by the detector and used to reconstruct the tomographic
images. Its energy is one of the most important factors in CT scanning, which thus affects

many other factors and configurations.

- The full absorption of X-ray photons relies on its energy, according to Figure 2.1 and Table 2.1. In other words, X-ray energy decides how deep the photon will penetrate the CZT crystal, or more clearly, X-ray energy used in clinical applications determine the thickness of detector.

- X-ray energy determines the initial distribution and the kinetic energy of its photo-electrons, as illustrated in Figure 2.3. To be more specific, higher energy X-rays are able to distribute energy further away from the original position of the interaction. This impacts a range of charge sharing effects and the collecting signal intensity.

- The proportion of different kinds of physical effects inside of the CZT detector, including *photoelectric effect*, *Compton scattering*, and *Rayleigh scattering*, rely on X-ray energy. No matter how thick the detector is, the proportions are unvarying when the X-ray energy is fixed, indicated in Figure 2.2 and Table 2.3. In detail, the proportion of the *photoelectric effect* is higher when X-ray energy is lower in the range between 10 keV and 140 keV. This means more interactions could be used to investigate the spatial resolution with lower energy X-ray photons.

- The proportion of *photoelectric effect*s on the different shells of different atoms in the CZT crystal vary with different X-ray energies, as shown in Figure 2.4. However, this is almost stable for X-rays with energy ranges from 50 keV to 140 keV.

In this thesis, 60 keV (Makeev *et al.*, 2013) and 120 keV (Aberle *et al.*, 2001) are selected to represent the applications for breast cancer and lung cancer diagnosis respectively.

4.1.2   Depth of Interaction

Depth of interaction (DOI) is the distance between the position that interaction takes place and the cathode plane. This equals the difference between the detector thickness and the distance the electron travels within the detector since all electrons will be collected by anodes ultimately.

- DOI influences the collected signal intensity. It determines the traveling distance and traveling time of the electrons within the detector. With smaller DOI, the traveling distance and the traveling time are longer. This means the electron cloud would expand wider and cast charge sharing effects on anodes more likely for the certain initial distribution.

- DOI affects the transit signal intensity as well. An electron has more potential energy and induces more transit signal on an anode with a smaller DOI, as shown in Figure 2.16 and Figure 2.17.

- DOI was decided by the X-ray energy. Generally, higher energy X-ray photons have larger DOIs. To be more specific, for the X-ray with energy 60 keV, the average DOI is 286.2 μm, while it is 1911 μm with 120 keV X-ray, according to Table 2.2.

DOI = 0.3 mm and DOI = 1.8 mm were selected for simulations in this thesis.

4.1.3   Lateral Offset of Interaction

The lateral offset (LO) of interaction decides which anode would be the collecting anode of the interaction. As analyzed in Chapter 3, almost all interactions would generate transit signals on both collecting anode and minor-collecting anodes, no matter how big the LO. Basically, weaker transit signal intensity always comes after a larger LO to the anode. However, for collecting signals, it becomes so important that the charge sharing effect only

occurs within a certain LO of interactions. This means there would be no collecting signal if the LO were too large.

4.1.4   Thickness of Detector

The thickness of the detector is the thickness of CZT crystal, which is the distance between anode plane and cathode plane.

- The most intuitive effect of thickness is on the proportion of full absorption of X-ray photons. According to Figure 2.1 and Table 2.1, full absorption proportion increases monotonically as thickness increased. For the 120 keV X-ray, 79.61% of all the photons would be fully absorbed by a 3 mm thick detector and 88.15% by a 4 mm thick detector. For 60 keV X-ray photons, 99.92% would be fully absorbed by a 2 mm thick detector and 100.00% if the detector thickness is equal to or greater than 3 mm.

- The thicker CZT detector works with lower radiation dosage for the patient, since higher full absorption proportion would bring more efficient usage of X-rays.

- A thicker detector also means longer traveling distance and traveling time for the electrons. Thus is more likely to cause trapping effects and broaden the electron cloud followed by a charge sharing effect. Although charge sharing effects deteriorate energy resolution, it can be used to achieve high spatial resolution in Chapter 3.

- Even though there could be benefit from a thicker CZT crystal, the caveat is a problem with engineering where larger crystals have more defects and higher cost.

In this thesis, the thickness of $L = 4\ mm$ was selected for most of the simulations.

4.1.5   Pitch Size

For the pixelated CZT detector, anode size and gap size both determine the appearance of the anode plane on the detector. Their sum is the pitch size. Basically, the pitch size affects the collecting signal more than the transit signal.

- The pitch size and the spatial resolution are positively correlated (in general).

  With smaller anode size, the profile of weighting potential is steeper when it comes close to the anode, and it has more ability to attract electrons, which is known as a small pixel effect (Figure 2.14). Generally, higher sub-pitch spatial resolution is achieved with smaller pitch size, which is the sum of anode size and gap size (discussed in Chapter 3).

- The pitch size should not be set too small.

  If this is done the broadened electron cloud might cover more than two pixels and cast charge sharing effect on all of them. For example, Figure 2.11 indicates that the range of *charge sharing effect* is ~ 111.5 μm while DOI $= 0.4$ mm and bias voltage $V = 300$ V with gap $g = 25$ μm. Thus, if the pitch size were $p \leqslant 111.5 + 25 = 136.5$ μm, the collecting signals would be generated on three pixels simultaneously resulting in failure to achieve sub-pitch spatial resolution with either method.

- The pitch size could not be set too large either. There are two kinds of situations here: too large of a gap size and too large of anode size.

  1. Too large gap size

     No charge sharing effect exists at all and two adjacent anodes could not output collecting signals for one interaction at the same time. For incidence, the upper limit for gap size depends on the range of the charge sharing effect with a certain bias voltage, such as $g_{ul} = 136.5$ μm with $V = 300$ V according to Figure 2.11.

2. Too large anode size

   Too small proportion of interactions could be used for achieving spatial resolu-tion with collecting signal. In the extreme case, if the gap size reaches its upper limit, the upper limit for anode size would be $a_{ul} = 1.347\ mm$ for keeping the proportion of charge sharing events no less than at least 15%. In other words, if the proportion of charge sharing events is expected to be no less than 15%, the upper limit for pitch size is $p_{ul} = 1583.5\ \mu m$.

In this thesis, an anode size of $a = 0.2\ mm$ (one twentieth of the selected thickness of the detector $L = 4\ mm$), and a gap size of $g = 50\ \mu m$ (one quarter of the selected anode size), were used as control configurations for the simulations.

4.1.6   Bias Voltage

The bias voltage is the potential difference applied between anode and cathode. It builds a constant electric field inside the detector, which attracts electrons to move toward anodes.

- Lower bias voltage means weaker electric field followed by longer traveling time for electrons with the same DOI, leading to higher likelihood for electron trapping. At the same time, the electron cloud widens with lower bias voltage as they travel certain distances towards the anode plane. The result is higher probability of generating collecting signal on more anodes due to charge sharing effect (Figure 2.12).

- If bias voltage were too large, leakage current between electrodes would become a problem. Fortunately, for all the models analyzed in this thesis, there was no issue with any bias voltage range from $100 \sim 900\ V$.

In this thesis, the bias voltage of $V = 300\ V$ was selected for all simulations.

4.2 Method for Investigating Spatial Resolution

In order to achieve sub-pitch spatial resolution with the pixelated CZT detector, two methods were investigated in this thesis. To begin with, interactions between X-ray photons and CZT crystal were simulated using a Monte-Carlo method in GATE, then the information concerning all interactions, including time, energy and position, were analyzed. Two kinds of signals on the anode, the collecting signal and transit signal, were evaluated separately.

4.2.1 Simulation in GATE

To obtain the events and interactions between different energy X-ray photons and CZT material in Section 2.2, a $100 \times 100 \times 100 \ mm^3$ CZT detector was modelled in GATE. It could fully absorb the X-ray photon's energy below 140 keV. At the same time, a 1 μm radius X-ray point source was set on the central line of the detector at a distance of 10 cm. The X-ray point source emits 5×10^5 X-ray photons within $\theta = 0$ and $\phi \in [0, 2\pi)$ for each energy step from 10 keV to 140 keV, with a 5 keV increment. To obtain interaction information to assess the signal on anodes, in Section 2.3 and Section 2.4, I repeated the simulations but moved the X-ray point source. Here the source emitted 60 keV or 120 keV X-ray photons, parallel to the anode plane, with discrete stopping positions (with the same acquisition times) every 10 μm.

The CZT material in all simulations was set to be $Cd_{0.9}Zn_{0.1}Te$. The space between the X-ray source and CZT crystal was set to be a vacuum and there was no collimator or phantom in this area. The interactions, including *photoelectric effect*, *Compton scattering*, *Rayleigh scattering*, and electron ionisation, were set based on a Penelope model. All information, such as time, energy and position, was saved in a "*.dat*" file.

4.2.2 Interactions of X-ray photons

Not all interaction events could be used to achieve sub-pitch spatial resolution with *intensity difference method* or *intensity ratio method*. Only single *photoelectric effect* events worked here. The proportion of single *photoelectric effect* events droped as X-ray photon energy increased (Figure 2.2). According to Table 2.3, 94.55% and 82.70% of all the interaction events with 60 *keV* and 120 *keV* X-rays, respectively, were useful, no matter how thick the detector.

Higher energy X-ray distributed its electron cloud further away from the original interaction position. It was 40 μm on average with 120 *keV* X-rays (Figure 2.5). The electron cloud would expand its radius during the time it moved towards anodes. It reached $r = 57$ μm at the anode plane when the depth of interaction DOI $= 0.3$ mm (Section 2.2.4).

4.2.3 Spatial Resolution Achieved

Two methods, the intensity difference method and intensity ratio method, were used to achieve sub-pitch spatial resolution (Chapter 3). Both methods have advantages and disadvantages.

- Transit signal

  After introducing the *Shockley-Ramo Theorem* (Section 2.4.1) and weighting potential (Section 2.4.2), I was able to estimate the transit signals. The weighting potential matrix was obtained with different anode size models, or more specifically, different ratio of the thickness of detector to anode size. Also, the transit signal intensities both on the collecting anode and neighboring minor-collecting anode were estimated with different anode size, gap size, DOI, as well as lateral offset, which made it possible to be used in achieving sub-pitch spatial resolution.

  Finally, for anode size of $a = 0.2$ mm and gap size of $g = 50$ μm, spatial resolution

of $SP \in (30, 40)$ μm was achieved with the *intensity difference method*, while it was $SP \in (20, 30)$ μm using the *intensity ratio method*.

It has to be pointed out that gap size is not as important as anode size when the spatial resolution was evaluated with transit signal. Although the spatial resolution achieved with transit signal was not as good as with collecting signal, the methods could be applied to almost all the *photoelectric effect* events and cover almost all lateral positions inside of detector with the transit signal.

- Collecting signal

  After assessment of the electron cloud density, comparing it to its initial distribution (Section 2.2.4), it was able to be used to estimate the collecting signals. A method to estimate the proportion of charge sharing events was introduced in Section 2.3.1. The ranges of charge sharing effect with different gap sizes and bias voltages were evaluated in Section 2.3.2. Furthermore, the collecting signal intensities, on two adjacent anodes were also estimated (Section 2.3.3), which made it possible to be used for achieving sub-pitch spatial resolution.

  Finally, with gap size of $g = 50$ μm, spatial resolution of $SP \in (10, 20)$ μm was achieved both with the *intensity difference method* and the *intensity ratio method*. However, based on simulation, resolution should be better with the latter.

  It has to be pointed out that anode size is not as important as gap size, when evaluating spatial resolution based on collected signal. But the ratio of anode size to gap size would affect the proportion of interaction events that could be used in both methods. For example, for a gap size of $g = 25$ μm, the proportion was 77.81%, 46.45% and 33.15% when the anode size $a = 0.2$ mm, $a = 0.4$ mm and $a = 0.6$ mm, respectively.

  Compared to transit signal, the collecting signal provides better spatial resolution, but it can only be used on *photoelectric effect* events taking place close to gaps.

With both two kinds of signals, *intensity ratio method* provides better spatial resolution than *intensity difference method* because of the removal of the influence of energy loss. In other words, the intensity function and the lateral position of interaction have a better linear relationship with the intensity ratio method.

4.3   Future Work

Although good enough spatial resolution was achieved after a series of investigations about factors inside pixelated CZT detectors, some other points need to be considered for future work. *Characteristic X-ray* would affect signals on anodes, especially for X-ray energies below 120 *keV*, which would be comparable to *characteristic X-ray*s themselves. Besides pixelated electrode CZT detectors, cross-strip electrode CZT detectors are also a popular type of photon counting detector. Thus their spatial resolution is also worthy of investigation. Lastly, in all simulations done throughout this thesis, all X-ray photons were assumed to hit the cathode vertically. This is obviously a far too ideal situation. Thus, investigation of incident projection angles away from $\pi/2$ would be a further worthy research direction.

Bibliography

Aberle, D. R., Gamsu, G., Henschke, C. I., Naidich, D. P., and Swensen, S. J. (2001). A consensus statement of the society of thoracic radiology: screening for lung cancer with helical computed tomography. *Journal of thoracic imaging*, **16**(1), 65–68.

Aberle D., Adams A., B. C. B. W. C. J. (2011). National lung screening trial research team and others. reduced lung-cancer mortality with low-dose computed tomographic screening. *N Engl J Med*, **2011**(365), 395–409.

Allison, J., Amako, K., Apostolakis, J. e. a., Araujo, H., Dubois, P. A., Asai, M., Barrand, G., Capra, R., Chauvie, S., Chytracek, R., *et al.* (2006). Geant4 developments and applications. *IEEE Transactions on Nuclear Science*, **53**(1), 270–278.

Allwork, C., Kitou, D., Chaudhuri, S., Sellin, P. J., Seller, P., Veale, M. C., Tartoni, N., and Veeramani, P. (2012). X-ray beam studies of charge sharing in small pixel, spectroscopic, cdznte detectors. *IEEE Transactions on Nuclear Science*, **59**(4), 1563–1568.

Beam, W. R. (1965). Electronics of solids.

Bushberg, J., Seibert, J., Leidholdt Jr, E., and Boone, J. (2003). *The essential physics of medical imaging. 2002.*, volume 30. Springer.

Bushberg, J. T. and Boone, J. M. (2011). *The essential physics of medical imaging.* Lippincott Williams & Wilkins.

Buzug, T. M. (2008). *Computed tomography: from photon statistics to modern cone-beam CT*. Springer Science & Business Media.

CCS (2016). Canadian cancer society's advisory committee on cancer statistics. Canadian Cancer Statistics 2016. Toronto, ON: Canadian Cancer Society.

Center, M., Siegel, R., and Jemal, A. (2011). Global cancer facts & figures. *Atlanta: American Cancer Society*, pages 1–52.

Chadder, J., Dewar, R., Shack, L., Nishri, D., Niu, J., and Lockwood, G. (2016). A first look at relative survival by stage for colorectal and lung cancers in canada. *Current Oncology*, **23**(2), 119.

Chen, W., Zheng, R., Baade, P. D., Zhang, S., Zeng, H., Bray, F., Jemal, A., Yu, X. Q., and He, J. (2016). Cancer statistics in china, 2015. *CA: a cancer journal for clinicians*, **66**(2), 115–132.

Cherry, S. R., Sorenson, J. A., and Phelps, M. E. (2012). *Physics in nuclear medicine*. Elsevier Health Sciences.

Ding, H., Ducote, J. L., and Molloi, S. (2012). Breast composition measurement with a cadmium-zinc-telluride based spectral computed tomography system. *Medical physics*, **39**(3), 1289–1297.

dAillon, E. G., Tabary, J., Glière, A., and Verger, L. (2006). Charge sharing on monolithic cdznte gamma-ray detectors: A simulation study. *Nuclear Instruments and Methods in Physics Research Section A: Accelerators, Spectrometers, Detectors and Associated Equipment*, **563**(1), 124–127.

Glick, S. J. (2014). Breast ct. *Cone Beam Computed Tomography*, page 235.

GLICK, S. J. and DIDIER, C. (2011). The effect of characteristic x-rays on the spatial and spectral resolution of a czt based detector for breast ct. *Progress in biomedical optics and imaging*, **12**(30).

He, Z. (2001). Review of the shockley–ramo theorem and its application in semiconductor gamma-ray detectors. *Nuclear Instruments and Methods in Physics Research Section A: Accelerators, Spectrometers, Detectors and Associated Equipment*, **463**(1), 250–267.

Iniewski, K., Chen, H., Bindley, G., Kuvvetli, I., and Budtz-Jorgensen, C. (2007). Modeling charge-sharing effects in pixellated czt detectors. In *2007 IEEE Nuclear Science Symposium Conference Record*, volume 6, pages 4608–4611. IEEE.

Jan, S., Santin, G., Strul, D., Staelens, S., Assie, K., Autret, D., Avner, S., Barbier, R., Bardies, M., Bloomfield, P., *et al.* (2004). Gate: a simulation toolkit for pet and spect. *Physics in medicine and biology*, **49**(19), 4543.

Kalemci, E. and Matteson, J. (2002). Investigation of charge sharing among electrode strips for a cdznte detector. *Nuclear Instruments and Methods in Physics Research Section A: Accelerators, Spectrometers, Detectors and Associated Equipment*, **478**(3), 527–537.

Kalluri, K., Glick, S. J., and Mahd, M. (2011). Snr improvement in dedicated breast ct using energy weighting with photon counting detectors. In *2011 IEEE 37th Annual Northeast Bioengineering Conference (NEBEC)*.

Kalluri, K. S., Mahd, M., and Glick, S. J. (2013). Investigation of energy weighting using an energy discriminating photon counting detector for breast ct. *Medical physics*, **40**(8), 081923.

Knoll, G. F. (2010). *Radiation detection and measurement.* John Wiley & Sons.

Krause, M. O. (1979). Atomic radiative and radiationless yields for k and l shells. *Journal of physical and chemical reference data*, **8**(2), 307–327.

Makeev, A., McGrath, J., Clajus, M., Snyder, S., and Glick, S. J. (2013). Achieving sub-pixel resolution using czt-based photon counting detectors for dedicated breast ct. In *SPIE Medical Imaging*, pages 86680T–86680T. International Society for Optics and Photonics.

NCI (2016). Cancer statistics. Website: https://www.cancer.gov/about-cancer/understanding/statistics.

Radon, J. (2005). 1.1 über die bestimmung von funktionen durch ihre integralwerte längs gewisser mannigfaltigkeiten. (on the determination of functions from their integrals along certain manifolds.). *Classic papers in modern diagnostic radiology*, **5**.

Ramo, S. (1939). Currents induced by electron motion. *Proc. Ire*, **27**(9), 584–585.

Shikhaliev, P. M. and Fritz, S. G. (2011). Photon counting spectral ct versus conventional ct: comparative evaluation for breast imaging application. *Physics in medicine and biology*, **56**(7), 1905.

Shikhaliev, P. M., Fritz, S. G., and Chapman, J. W. (2009). Photon counting multienergy x-ray imaging: Effect of the characteristic x rays on detector performance. *Medical physics*, **36**(11), 5107–5119.

Shockley, W. (1938). Currents to conductors induced by a moving point charge. *Journal of applied physics*, **9**(10), 635–636.

Siegel, R. L., Miller, K. D., and Jemal, A. (2016). Cancer statistics, 2016. *CA: a cancer journal for clinicians*, **66**(1), 7–30.

Veale, M. C., Bell, S. J., Jones, L. L., Seller, P., Wilson, M. D., Allwork, C., Kitou, D., Sellin, P. J., Veeramani, P., and Cernik, R. C. (2011). An asic for the study of charge sharing effects in small pixel cdznte x-ray detectors. *IEEE Transactions on Nuclear Science*, **58**(5), 2357–2362.

Zheng, X., Cheng, Z., Deen, M. J., and Peng, H. (2016). Improving the spatial resolution in czt detectors using charge sharing effect and transient signal analysis: Simulation study. *Nuclear Instruments and Methods in Physics Research Section A: Accelerators, Spectrometers, Detectors and Associated Equipment*, **808**, 60–70.